PONTIFICIA UNIVERSIDAD CATOLICA DE CHILE

ESCUELA DE INGENIERIA

REPROCESSING SCINTILLOMETER DATA ALTERED BY WIND CURRENTS TO DESCRIBE EVAPOTRANSPIRATION FLUXES IN A SEMI-ARID REGION

FRANCISCA AGUIRRE CORREA

Thesis submitted to the Office of Research and Graduate Studies in partial fulfillment of the requirements for the Degree of Master of Science in Engineering.

Advisor:

FRANCISCO SUÁREZ POCH

Santiago de Chile, January, 2021

PONTIFICIA UNIVERSIDAD CATOLICA DE CHILE

ESCUELA DE INGENIERIA

REPROCESSING SCINTILLOMETER DATA ALTERED BY WIND CURRENTS TO DESCRIBE EVAPOTRANSPIRATION FLUXES IN A SEMI-ARID REGION

FRANCISCA AGUIRRE CORREA

Members of the Committee:

FRANCISCO SUÁREZ POCH
WERNHER BREVIS VERGARA
FRANCISCO MEZA DABANCENS
OSCAR HARTOGENSIS
RICARDO GIESEN ENCINA

Thesis submitted to the Office of Research and Graduate Studies in partial fulfillment of the requirements for the Degree of Master of Science in Engineering.

Santiago de Chile, January, 2021

ACKNOWLEDGMENTS

Firstly, I would like to thank my advisor Francisco Suárez for supporting me throughout all this experience and always inspiring me to bring my knowledge beyond what I believe I can do. Secondly, I specially thank Oscar Hartogensis from Wageningen & Research University, the Netherlands, as without his help this work would not have been possible. Your expertise and knowledge, along with your kindness, allowed me to enter this very unknown world of scintillometry. Thank you both for trusting my abilities to carry out this research even more than I did myself.

Thanks to my parents and family for supporting my decisions and encouraging me to work hard to reach my goals. Thanks to Vicente, Catalina, Francisco and Fernanda for being there for me during these last past months. Without you I would probably have given up on this path. Thanks to everyone I met throughout this journey and the ones who were present from the beginning, especially my high school friends and Macarena.

Finally, I thank the Agencia Nacional de Investigación y Desarrollo (ANID) for funding grants FONDECYT/1170850, FONDECYT/1170429 and FONDEQUIP/EQM170024, as well as the Centro de Desarrollo Urbano Sustentable (CEDEUS – ANID/FONDAP/15110020) and the Centro de Excelencia en Geotermia de los Andes (CEGA – ANID/FONDAP/15090013) for supporting this investigation.

CONTENTS

LIST OF TABLES

LIST OF FIGURES

ABSTRACT

Evapotranspiration (ET) is a key component of the hydrological cycle, being relevant for water management in arid and semiarid regions under a changing climate. ET links water and energy budgets in the form of latent heat (L_vE) released to the atmosphere. However, ET is difficult to measure, especially in heterogeneous fields where vegetation is sparse and where irrigated crops are surrounded by heterogeneous surfaces that provide additional energy to the system. Thus, ET is the not always well described in arid regions being necessary to incorporate novel techniques for its accurate measurement. Lately, studies have reported good results using scintillometers. They work better in heterogeneous regions and over large spatial scales. However, scintillometer signals can present unwanted contributions which overestimate heat fluxes. In this study, scintillometer data altered by wind currents showed unrealistic heat flux values and thus, these data were reprocessed through spectral analysis to eliminate unwanted contributions from electronic noise, absorption and tripod vibrations. After a spectral cleaning, scintillometer-based heat fluxes were calculated using several methods: i) energy balance closure, ii) Hill model, iii) Lüdi et al. model , and iv) Hybrid model. Corrected sensible heat flux (H) estimations agreed well with those obtained with an Eddy Covariance (EC) system. However, considerable differences were found for L_vE (and consequently ET), when using the different methods. The Lüdi et al. model L_vE estimates were closer to those obtained with the EC system, overestimating it in ~14% with a correlation slope of 1.07 and a coefficient of determination of 0.91. Also, it was found that using different similarity functions results in more than ±12% of difference on the estimated L_vE. For future works it is strongly recommended to apply spectral cleaning as it greatly improves scintillometer data, as well as to ensure tripod stability and correct alignment when performing scintillometer measurements.

Keywords: optical scintillometer, microwave scintillometer, tripod vibration filter, spectral analysis, evapotranspiration.

RESUMEN

La evapotranspiración (ET) es un componente clave del ciclo hidrológico, siendo relevante para la gestión del agua en regiones áridas y semiáridas bajo un clima cambiante. La ET vincula los balances de agua y energía en forma de calor latente (L_vE) liberado a la atmósfera. Sin embargo, la ET es difícil de medir, especialmente en campos heterogéneos donde la vegetación es escasa y donde los cultivos de regadío están rodeados de superficies heterogéneas que aportan energía adicional al sistema. Así, la ET no siempre es bien descrita en regiones áridas, siendo necesario incorporar técnicas novedosas para su medición. Últimamente, estudios han reportado buenos resultados obtenidos con el uso de escintilómetros. Funcionan mejor en regiones heterogéneas y a grandes escalas espaciales. Sin embargo, las señales de los escintilómetros pueden presentar contribuciones no deseadas que sobrestiman los flujos de calor. En este estudio, datos de escintilómetro alterados por corrientes de viento entregaron flujos de calor poco realistas y, por tanto, estos datos fueron reprocesados mediante un análisis espectral para eliminar contribuciones no deseadas de ruido electrónico, absorción y vibraciones del trípode. Tras una limpieza espectral, se calcularon los flujos de calor utilizando varios métodos: i) cierre del balance energético, ii) modelo de Hill, iii) modelo de Lüdi et al. y iv) modelo híbrido. Las estimaciones de flujo de calor sensible (H) concordaron bien con las obtenidas con un sistema *Eddy Covariance* (EC). Sin embargo, se encontraron diferencias considerables para el L_vE (y, en consecuencia, la ET), al utilizar los distintos métodos. Las estimaciones de L_vE de Lüdi et al. se aproximaron más a las obtenidas con el sistema EC, sobrestimándola en un ~14% con una pendiente de correlación de 1,07 y un coeficiente de determinación de 0,91. Además, se comprobó que el uso de diferentes funciones de similitud da lugar a más de un ±12% de diferencia en el L_vE estimado. Para futuros trabajos se recomienda siempre aplicar la limpieza espectral, ya que mejora en gran medida los datos de escintilómetros, así como asegurar la estabilidad del trípode y la correcta alineación al realizar las mediciones.

Palabras clave: escintilómetro óptico, escintilómetro de microondas, filtro de vibración de trípodes, análisis espectral, evapotranspiración.

1 Introduction

To improve water management in arid regions under a changing climate it is important to understand the hydrological, atmospheric, and climatic processes that participate in the water and energy cycles. Evapotranspiration (ET) is a critical component of the hydrological cycle, but it is the not always well characterized in arid and semi-arid regions (Lemeur & Zhang, 1990; Parasuraman et al., 2007; Chovanes et al., 2020). ET links water and energy budget via latent heat (L_vE) released to the atmosphere. ET measurements are difficult to obtain, especially in agricultural fields where irrigated crops tend to be surrounded by heterogeneous surfaces that could provide additional energy to the system (Figuerola & Berliner, 2005). Therefore, studies have investigated different methods to obtain proper ET estimates (Lemeur & Zhang, 1990; Zhang et al., 2008; Mohawesh, 2011; Li et al., 2016).

The two most popular approaches for obtaining direct ET estimations are water budget and water vapor transfer methods. Water budget methods include pan evaporation, water balance of basin, lysimetry and soil moisture depletion, whereas water vapor transfer methods include the Bowen ratio-energy budget and the Eddy Covariance (EC) techniques. EC is the most widely accepted by the scientific community for field-scale measurements (Shuttleworth, 2008; Zhang et al., 2008; Ellsäber et al., 2020), although new promising techniques have been developed.

On one hand, EC systems measure fluctuations of wind speed, temperature, and water vapor at high frequency (10-20 Hz) to estimate sensible heat flux (H) and L_vE. EC is the best method used to measure the Bowen ratio, i.e., L_vE/H, with ET deduced from the surface energy budget. However, its main disadvantages are: (1) the measured fluxes are not necessarily representative of those occurring over large and heterogeneous surfaces (Stoffer, 2018), (2) flow distortion by the mast or the instrument itself in unfavorable wind directions yields inaccurate flux measurements (van Kesteren et al., 2013), and (3) it has shown a systematic underestimation of fluxes (Shuttleworth, 2008). Recent studies have shown that scintillometers are an interesting alternative for traditional methods, such as EC, especially for heterogeneous and

natural landscapes, and over large spatial scales (Meijninger et al., 2002; Yee et al., 2015). Scintillometers use the Monin-Obukhov similarity theory (MOST; Monin and Obukhov, 1954) and universal similarity functions to estimate area-averaged H and L_vE at 0.1-10 km spatial scales (van Kesteren et al., 2013). They use different theoretical methods to compute ET from electromagnetic waves, such as the energy balance closure method (Ezzahar et al., 2009), the Hill's (1997) method, the Lüdi et al. (2005) method, and the hybrid method (Stoffer, 2018). This technology overcomes many of the limitations of EC systems as it does not suffer from flux distortion, it obtains representative fluxes for larger scales and it has been successfully used in heterogeneous terrains (Meijninger et al., 2005). However, its main disadvantage is that H and L_vE are determined indirectly, which can lead to errors. For instance, scintillometers present unwanted contributions to the signal from electronic noise and absorption that must be filtered to obtain accurate heat fluxes estimations (Stoffer, 2018). Also, there is no consensus on the exact form of the MOST universal similarity functions (Kooijmans and Hartogensis, 2016). Hence, proper selection of these functions is important for correct estimation of H and L_vE.

Recent data have shown that scintillometer results may be biased. For example, during a field campaign in a vineyard in Pirque, Chile (Luque et al., 2019), it was found that tripods where scintillometers were installed vibrated due to wind currents. These vibrations added important unwanted contributions to the scintillometer signal. This issue considerably altered the data resulting in unrealistic overestimations of heat fluxes. Hence, this work addresses the following research questions:

1. How wind currents affect scintillometer-based heat fluxes?

2. How the state-of-the-art filtering process (Stoffer, 2018) can be improved to also include filtering of tripod vibrations as unwanted contributions?

3. Which of the different theoretical methods that are used to estimate heat fluxes with scintillometers yields better results?

4. What is the impact of using different MOST similarity functions on scintillometer-based heat fluxes? Can new MOST similarity functions be proposed that work better for the conditions observed at the vineyard in Pirque?

1.1 Objectives

The general objective of this work is to evaluate scintillometers performance to measure heat fluxes in a Chilean vineyard in comparison with the currently preferred EC method. To achieve this general objective, four specific objectives will be addressed:

1. To investigate how scintillometer-based heat fluxes could be overestimated, compared to EC measurements, when subject to wind currents.

2. To study how scintillometer data altered by wind currents during the field campaign in Pirque (Luque et al., 2019) can be reprocessed by improving Stoffer (2018) filtering process.

3. To assess the impact of different scintillometer theoretical methods on scintillometer heat fluxes using the cleaned data.

4. To evaluate the impact of using different MOST similarity functions on scintillometer-based heat fluxes, and to propose new MOST similarity functions for the conditions observed in the field experiment (Luque et al., 2019).

1.2 Thesis structure

The structure of this thesis is as follows. Chapter 1 corresponds to the introduction, where the research questions and objectives are state. Chapter 2 describes the materials and methods used in this research. Then, section 2.1 shows the scintillometer theory, section 2.2 describes the data obtained during the field campaign in the vineyard in

Pirque and section 2.3 presents the methods used to achieve the specific objectives shown above. Chapter 3 shows the results, including the spectral filtering process, the corrected surface heat fluxes using the four different theoretical methods and the MOST analysis. Chapter 4 presents the discussion of the results, chapter 5 the main conclusions, and finally the references are cited in chapter 6. An appendix with useful information is presented at the end of this report.

2 Materials and methods

2.1 Measurement principle of scintillometers

The functioning of a scintillometer consists of a transmitter that emits a light beam through the atmosphere to a receiver located at some distance, which records the intensity of the signal. This light beam is an electromagnetic wave with a certain wavelength that typically varies between the optical and microwave ranges. Scintillometers that work at optical wavelengths are called Large Aperture Scintillometers (LAS), while scintillometers that work at microwave wavelengths are named Microwave Scintillometers (MWS). The combination of these two scintillometers is known as the Optical Microwave Scintillometer (OMS).

On their path length, i.e., the distance between receiver and transmitter, the light beam passes through turbulent eddies with differences in temperature, humidity, and refractive index, making the signal scatter. Thus, signal scatter is proportional to atmospheric turbulence. This scattering is detected as intensity fluctuations in the receiver (van Kesteren, 2012; Yee et al., 2015), as shown in Figure 2-1. When combining theoretical principles of atmospheric turbulence with the physics of electromagnetic wave propagation -estimated indirectly from intensity fluctuations measured on the receiver as variances ($\sigma_{ln}^2{}_{(I)}$)-, it is possible to obtain H and L_vE (Hill, 1989; Li et al., 2012a). The atmospheric turbulence is quantified by structural parameters, which allows to obtain heat fluxes from $\sigma_{ln}^2{}_{(I)}$. The structural parameters

are a measure of the turbulent energy present in the inertial range of the refractive index (C_n^2 [$m^{-2/3}$]), temperature (C_T^2 [$K^2 m^{-2/3}$]), specific humidity (C_q^2 [$kg^2/kg\ m^{-2/3}$]), and temperature-humidity correlation (C_{Tq} [$kg/kg\ Km^{-2/3}$]), and depend on the specific wavelength λ of the light beam (Wang et al., 1978).

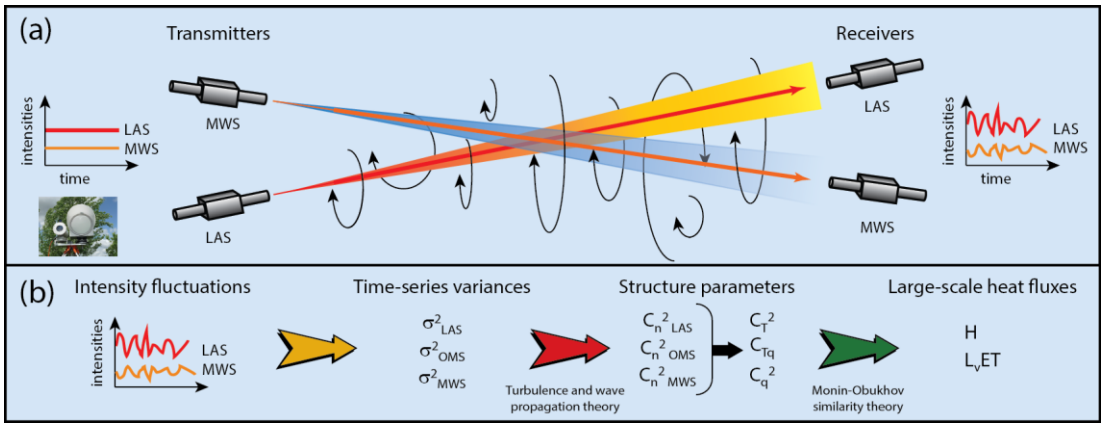

Figure 2-1: Schematic representation of the methodology used to determine sensible and latent heat fluxes using OMS. (a) Representation of the turbulent field that interacts with the scintillation signals. (b) Workflow diagram used to determine sensible and latent heat fluxes using the OMS.

Using a precise description of the refractive index spectrum, the total contribution to $\sigma_{ln}^2{}_{(I)}$ can be obtained from the contribution of each eddy within the path length. According to Wang et al. (1978), the analytical solutions that relate $\sigma_{ln}^2{}_{(I)}$ and C_n^2 for different wavelengths (λ_{opt} = 0.85 μm (Kipp & Zonen, 2020) and λ_{mw} = 1.86 mm (RPG Radiometer Physics, 2015) for the optical and microwave range, respectively) can be written as:

$$\sigma^2_{\ln(I),opt} = c_{opt} D^{\frac{-7}{3}} L^3 C^2_{n,opt} \quad (1)$$

$$\sigma^2_{\ln(I),mw} = c_{mw} F^{\frac{-7}{3}} L^3 C^2_{n,mw} \quad (2)$$

$$\sigma^2_{\ln(I),opt,mw} = c_{opt,mw} max(D,F)^{\frac{-7}{3}} L^3 C^2_{n,opt,mw} \quad (3)$$

in which c_{opt}, c_{mw} and $c_{opt,mw}$ are constants [-] where the subindices *opt*, *mw* and *opt,mw* refer to optical, microwave, and optical-microwave, L is the path length [m], D is the optical scintillometer diameter [m] and $F = \sqrt{\lambda L}$ is the Fresnel length [m]. Then, C_n^2 is estimated by the $\sigma_{ln}^2{}_{(I)}$ measured in the receiver.

However, heat fluxes are not directly related to C_n^2 but to the temperature structural parameter C_T^2 for estimating H, and to the humidity structural parameter C_q^2 for estimating L_vE. Hill (1997) derived empirical formulas that relate the C_n^2 to the structural parameters C_T^2, C_q^2 and C_{Tq} by applying the Reynolds' decomposition:

$$C_n^2 = \frac{A_T^2}{\bar{T}^2} C_T^2 + \frac{2A_T A_q}{\overline{T_q}} C_{T_q} + \frac{A_q^2}{\bar{q}^2} C_q^2 \tag{4}$$

where T is temperature [K], q is specific humidity [kg/kg], and A_i are dimensionless coefficients [-] dependent on atmospheric pressure, temperature and specific humidity (see Appendix A). Overbars denote mean values over a temporal interval. In equation (4), C_T^2, C_q^2, and C_{Tq} are independent of the light beam wavelength, while the rest are dependent of it.

Green et al. (2001) found that the LAS is sensitive to temperature fluctuations and therefore to C_T^2, while the MWS is sensitive to both temperature and humidity fluctuations, but more sensitive to C_q^2. In both cases C_{Tq} is not negligible. Since LAS is more sensitive to C_T^2 and little information is usually available on C_{Tq} and C_q, additional information on the relationship between T and q fluctuations is used when using a standalone LAS (Wesely, 1976). For this, Moene (2003) added a correction to the effect of C_q and C_{Tq} over C_n^2, known as the Bowen's correction, which assumes that the correlation coefficient between the temperature and humidity fluctuations (r_{Tq} [-]) is ±1:

$$C_n^2 = \frac{A_T^2}{\bar{T}^2} C_T^2 \left(1 + \frac{A_q}{\bar{q}} \frac{\bar{T}}{A_T} \frac{c_p}{L_v} \beta^{-1}\right)^2 \tag{5}$$

where β is the Bowen ratio and c_p the specific heat at constant pressure. Therefore, LAS allows calculation of H [W/m^2] without making measurements or assumptions about humidity fluctuations (Yee et al., 2015). However, L_vE [W/m^2] cannot be estimated directly since C_q^2 is disregarded. Thus, the surface energy balance closure (EBC) is typically used to obtain L_vE after H has been estimated (Culf et al., 2013):

$$R_n - G = H + L_vE \tag{6}$$

where R_n is net radiation [W/m^2] and G is the ground heat flux [W/m^2]. As a convention, it is considered that R_n is positive when directed into the surface, while the other fluxes are positive when directed away from it (see Figure A.2 in Appendix A).

When using an OMS, both H and L_vE can be obtained simultaneously without the need of closing the surface energy balance. In this case, equation (4) can be written for each operating wavelength. As a result, there are two equations (for $C_n{}^2{}_{opt}$ and $C_n{}^2{}_{mw}$) and three unknowns, which corresponds to the meteorological structural parameters ($C_T{}^2$, $C_q{}^2$ and C_{Tq}). Thus, three approaches have been proposed to find the structural parameters.

The first approach, also known as the two-wavelength method, was proposed by Hill (1997). It consists of assuming that the three structural parameters are not independent, and that the r_{Tq}, defined in equation (7), is ± 1 (positive for the unstable conditions that occur during day and negative for the stable conditions that occur during night):

$$r_{Tq} = \frac{C_{Tq}}{\sqrt{C_T^2 C_q^2}} \tag{7}$$

Many investigations have used the two-wavelength method (Andreas et al., 1989; Green et al., 2001; Kohsiek and Herben, 1983; Meijninger et al., 2002). However, for non-ideal flows, assuming $r_{Tq} = \pm 1$ is not always valid, especially over heterogeneous terrain (Lüdi et al., 2005) as the MOST assumptions are infringed. For this reason, Lüdi et al. (2005) proposed using 0.8 for day and -0.6 for night when using Hill's (1997) method.

The second approach, also known as the bichromatic method, was proposed by Lüdi et al. (2005). This approach is based on the covariance between the LAS and MWS signals to derive the C_{Tq}. The path-averaged C_{Tq} is found by cross-correlating the two electromagnetics signals at different wavelengths that pass through the same air volume (Lüdi et al., 2005). This approach has the advantage that no assumptions are made to find C_{Tq}. However, the bichromatic approach is less robust than the two-wavelength method as sometimes it delivers chaotic behaviour or unrealistic r_{Tq} values (Lüdi et al. 2005; Stoffer, 2018). In this method, the equations required to find the three structural meteorological parameters are the two versions of equation (4), written for each operating wavelength, and equation (7).

The most recent approach to find the structural parameters, also known as the hybrid method, was developed by Stoffer (2018). This approach uses corrected r_{Tq} values estimated from the Lüdi et al. (2005) method, and applies them in the Hill (1997) method to compute heat fluxes. This procedure reduces the chaotic behaviour of the r_{Tq} values obtained from the Lüdi et al. (2005) method, and it produces more robust results than those obtained in the Hill (1997) method (Stoffer, 2018).

Once the meteorological structural parameters are found, C_T^2 and C_q^2 can be directly related to H and L_vE, respectively, through the MOST. MOST describes the characteristics of turbulence in the atmospheric surface layer, relating the measured turbulence statistics to temperature, humidity, and wind scales. These magnitudes are defined in terms of the turbulent fluxes of heat (H), moisture (L_vE), and momentum

(τ). In MOST, C_T^2 and C_q^2 scale with $\theta_*^2/(z-d)^{2/3}$ and $q_*^2/(z-d)^{2/3}$, respectively, through the MOST universal similarity functions $f_{C_T^2}$ and $f_{C_q^2}$:

$$\frac{C_T^2(z-d)^{2/3}}{\theta_*^2} = f_{C_T^2}\left(\frac{z-d}{L_O}\right) \tag{8}$$

$$\frac{C_q^2(z-d)^{2/3}}{q_*^2} = f_{C_q^2}\left(\frac{z-d}{L_O}\right) \tag{9}$$

where θ_* [K] and q_* [kg/kg] are the temperature and specific humidity turbulent scales, z is the beam effective height [m], d is the zero-plane displacement [m], and L_O is the Obukhov length [m], which represents the height above the surface where friction and convective turbulence production are equal. L_O is estimated as:

$$L_O = -\frac{T}{\kappa g}\frac{u_*^2}{\theta_*} \tag{10}$$

where κ is the von Kármán constant (0.4), g is gravity (9.8 m/s^2) and u_* is the friction velocity [m/s]. Although $f_{C_T^2}$ and $f_{C_q^2}$ are assumed to be universal, it has been shown that different MOST functions can cause up to 20% difference in H estimations (Hartogensis et al., 2003). Wyngaard et al. (1971) found general similarity functions for unstable ($z/L_O < 0$) and stable ($z/L_O > 0$) conditions:

$$f_{C_{T\,unstable}^2}\left(\frac{z-d}{L_O}\right) = c_{T1}\left(1 - c_{T2}\frac{z-d}{L_O}\right)^{-2/3} \tag{11}$$

$$f_{C_{q\,unstable}^2}\left(\frac{z-d}{L_O}\right) = c_{q1}\left(1 - c_{q2}\frac{z-d}{L_O}\right)^{-2/3} \tag{12}$$

$$f_{C_{T\,stable}^2}\left(\frac{z-d}{L_O}\right) = c_{T1}\left(1 + c_{T2}\left(\frac{z-d}{L_O}\right)^{-2/3}\right) \tag{13}$$

$$f_{C_{q\,stable}^2}\left(\frac{z-d}{L_O}\right) = c_{q1}\left(1 + c_{q2}\left(\frac{z-d}{L_O}\right)^{-2/3}\right) \tag{14}$$

where c_{Ti} and c_{qi} are empirical coefficients. As shown in Table 2-1, there are many MOST functions in the scientific literature.

Table 2-1: Coefficients for $f_{C_T^2}$ and $f_{C_q^2}$ MOST functions. The Kooijmans and Hartogensis (2016) similarity coefficients were applied when the humidity coefficients were not available.

	$f_{C_T^2}$				$f_{C_q^2}$			
	Stable		**Unstable**		**Stable**		**Unstable**	
Author	c_{T1}	c_{T2}	c_{T1}	c_{T2}	c_{q1}	c_{q2}	c_{q1}	c_{q2}
Kooijmans and Hartogensis (2016)	5.5	1.1	5.6	6.5	4.5	1.1	4.5	7.3
Andreas (1988)	4.9	2.2	4.9	6.1	-	-	-	-
De Bruin et al. (1993) / Hartogensis and De Bruin (2005) [(1)]	4.7	1.6	4.9	9.0	-	-	-	-
Li et al. (2012a)	4.5	1.3	6.7	14.9	3.5	2.7	3.5	4.5
Wyngaard et al. (1971)	4.9	2.75	4.9	7.0	-	-	-	-

[(1)] For $f_{C_T^2}$, the De Bruin et al. (1993) similarity coefficients were used for unstable conditions, whereas the Hartogensis and De Bruin (2005) similarity coefficients were used for unstable conditions.

Finally, considering $H = \rho c_p \theta_* u_*$ and $L_v E = \rho L_v q_* u_*$, and combing them with equations (8) and (9), respectively, H and L_vE are obtained (Zhang et al., 2020).

$$H^2 = -\frac{\bar{\rho}^2 c_p^2 u_*^2 (z-d)^{2/3} C_T^2}{f_{C_T^2}} \tag{15}$$

$$L_v E^2 = -\frac{\bar{\rho}^2 L_v^2 u_*^2 (z-d)^{2/3} C_q^2}{(1-\bar{q})^2 f_{C_q^2}} \tag{16}$$

where ρ is the air density [kg/m^3]. For a complete explanation of scintillometer theory refer to Appendix A.

2.2 Study area and data collected

The study area is an irrigated vineyard located in Pirque; an agriculture-based province located in the semi-arid Central valley of Chile (Figure 2-2(a)). This region has a warm climate, with a summer period between December and February, with an average temperature of 20.1 °C, a maximum of 30.4 °C and a minimum of 12 °C. The winter period between June and August has an average temperature of 8.9 °C, maximum of 14.3 °C and minimum of 4.4 °C. The normal annual precipitation is 457 mm, with a minimum of 450 mm and a maximum of 466 mm. However, for 2050 precipitation is expected to decrease until 392 mm, while minimum and maximum temperature will increase in 2 °C (MMA-INFODEP, 2016).

A field campaign was performed between January 8th and 18th, 2019. An EC system (IRGASON, Campbell Scientific Inc, Logan, UT, USA) and a meteorological station were set up in the middle of the vineyard 4 m above ground (Figure 2-2(b)). The meteorological station includes a temperature and relative humidity sensor (HMP45C, Campbell Scientific Inc, Logan, UT, USA), a net radiometer (NR Lite 2, Kipp & Zonen, Delft, The Netherlands), four HFP01-L soil heat flux plates (HFP01-L, Campbell Scientific Inc., Logan, UT, USA), two soil thermocouples (TCAV, Campbell Scientific Inc., Logan, UT, USA), and a water content reflectometer (CS616, Campbell Scientific Inc., Logan, UT, USA) All these sensors were connected to a datalogger (CR3000, Campbell Scientific Inc., Logan, UT, USA).

As shown in Figure 2-2(b), an OMS was installed to estimate H and L_vE, with the main aim of determining ET fluxes at the plot scale. The OMS is composed of a LAS (LAS MkII, Kipp & Zonen, Delft, The Netherlands) with an aperture of 149 mm and a wavelength of 850 nm, and an MWS (RPG-MWSC-160, RPG Radiometer Physics GmbH, Meckenheim, Germany) with an aperture of 300 mm and a wavelength of 1.86 mm. The path length was 480 m, and the effective height was 3.02 m (calculated following the methods presented by Hartogensis et al., 2003). The zero-displacement height was 1.12 m, and the roughness caused by the crops was 0.2 m because the

vineyard was classified as a semiarid surface with tall crops and numerous obstacles (Hansen,1993). The zero-displacement height was estimated from the crop averaged height ($H_{veg} = 1.6\ m$) as $d = 0.7H_{veg}$ (Grimmond & Oke, 1999).

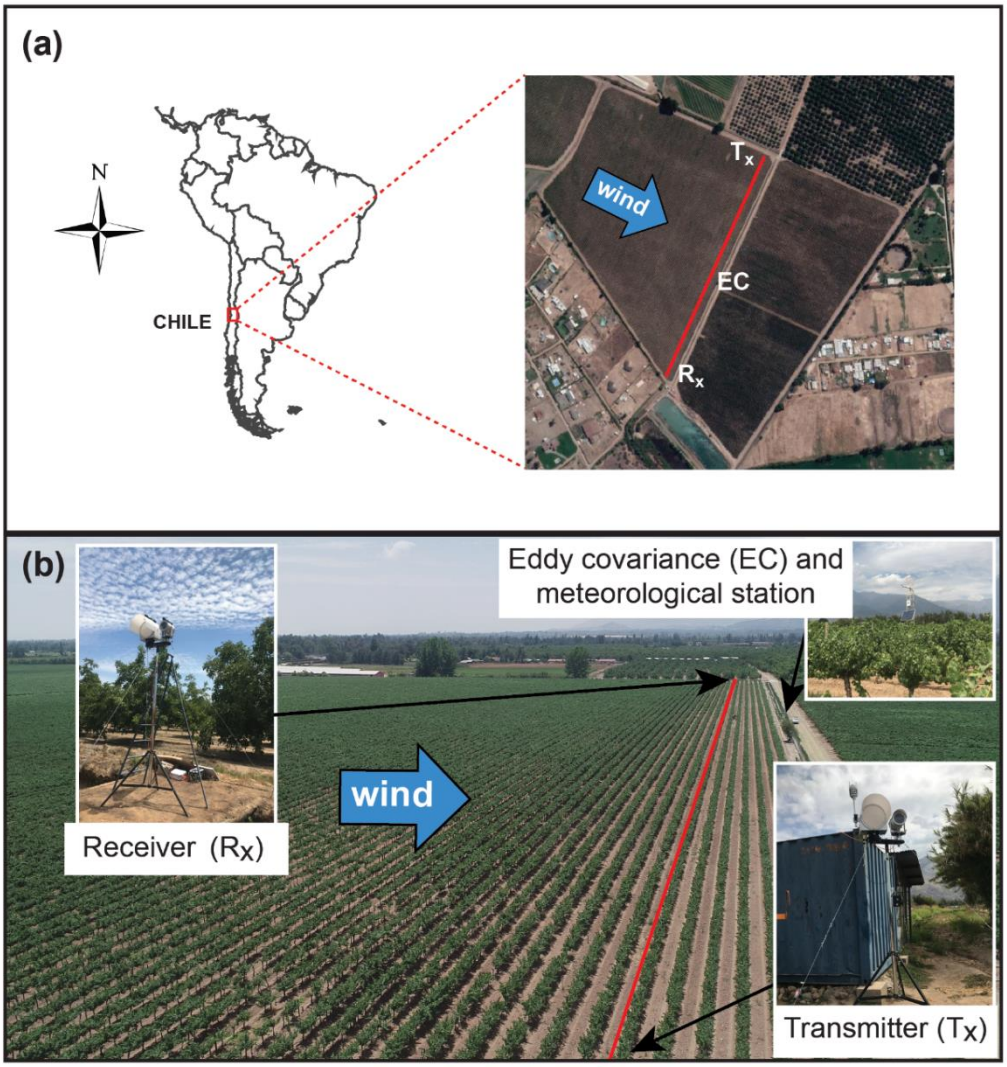

Figure 2-2: (a) Geographical location of study area (b) EC system and meteorological station, and OMS installed in the study area.

2.3 Identification of unwanted contributions related to wind and spectral cleaning

Unwanted contributions to the OMS signal can result in unrealistic heat fluxes. I hypothesize that tripod vibrations as a consequence of wind currents add important unwanted contributions to the signal within the scintillometer frequencies that results in overestimated H, L_vE, and consequently in the ET rates. Therefore, to obtain better estimates of the surface heat fluxes, the OMS signal must be cleaned before the determination of the meteorological structural parameters.

The first step to identify unwanted contributions to the scintillometer signal is by performing a spectral analysis. Spectral analysis is a powerful tool for describing turbulence and recognizing the frequencies that are most important for the signal. With the aim of relating these unwanted contributions to wind currents, an analysis of the averaged scintillometer signal along with the wind speed observed during the field campaign is carried out. The averaged signal is a good indicator of the signal quality since it is expected to be constant in time. Also, when the averaged signal is too low, the fluctuations cannot be measured correctly. Thus, by analysing if there is a coincidence between wind speed and the quality of the signal, wind can be stated as a cause for scintillometer measurements alteration. After finding the unwanted contributions, a spectral analysis cleaning process is performed by adapting the filtering method proposed by Stoffer (2018). He cut off unwanted contributions from electronic noise, absorption and erratic spikes from the frequency range. In the present study, I expanded the work of Stoffer (2018) by adding an approach to remove unwanted contributions related to tripod vibrations, as described below.

First, to eliminate signal contributions due to electronic noise and absorption, Stoffer (2018) recommends applying band pass filters to the original spectrum: a 0.1 Hz high pass filter (HPF) and a 100 Hz low pass filter (LPF). Thus, any frequency contribution below 0.1 Hz or above 100 Hz is cut off. Then, a filtering process of erratic spikes and unwanted contributions from tripod vibrations filtering is performed. This process is

not trivial as typically tripod vibration frequencies are within the scintillometer frequencies. Therefore, it needs to be carried out carefully to avoid filtering the correct signal that should be used by the LAS and MWS. Figure 2-3 presents a diagram that explains the algorithm used to filter erratic spikes and unwanted contributions due to tripod vibrations. It consists in dividing the spectrum in blocks of 5% of the total data and calculating the block's median (MED) and mean absolute deviation (MAD). Then, erratic peaks and tripod vibrations within the data block are defined when the following condition is met:

$$S_f > MED + aMAD \quad if \quad frequency \leq FT\ Hz \tag{17}$$

$$S_f > MED + bMAD \quad if \quad frequency > FT\ Hz \tag{18}$$

where S_f is the value of the spectrum in the frequency range, a and b are empirical coefficients, and FT is a frequency threshold [Hz]. The previous condition is a piecewise function, as opposed to what was proposed by Stoffer (2018), because low and high frequencies may have different unwanted contributions to the signal. Hence, the values of a and b must be defined for each dataset. The FT also needs to be selected for each set of data (e.g., 2 Hz generally is where tripod vibrations occur). When the erratic peaks of one data block are found, the next block to be analysed is overlapped to ensure continuity and the process is repeated until the unwanted contributions of all the blocks are found. To remove the unwanted contributions of erratic peaks and tripod vibrations, their Fourier coefficients are randomly varied by assuming that they distribute uniformly within each data block, so the relevant statistical properties are not modified. As this approach could produce new artificial erratic peaks, an iterative process is carried out until all the unwanted contributions are removed. Once the corrected spectrum without electronic noise, absorption, erratic spikes and unwanted contributions from tripod vibrations is obtained, the variance of the signal is calculated using the integral of the spectrum curve as the spectrum is scaled such that the area under the spectrum is proportional to the signal variance. Also, the corrected signal time series is estimated using the inverse Fourier fast transform (IFFT).

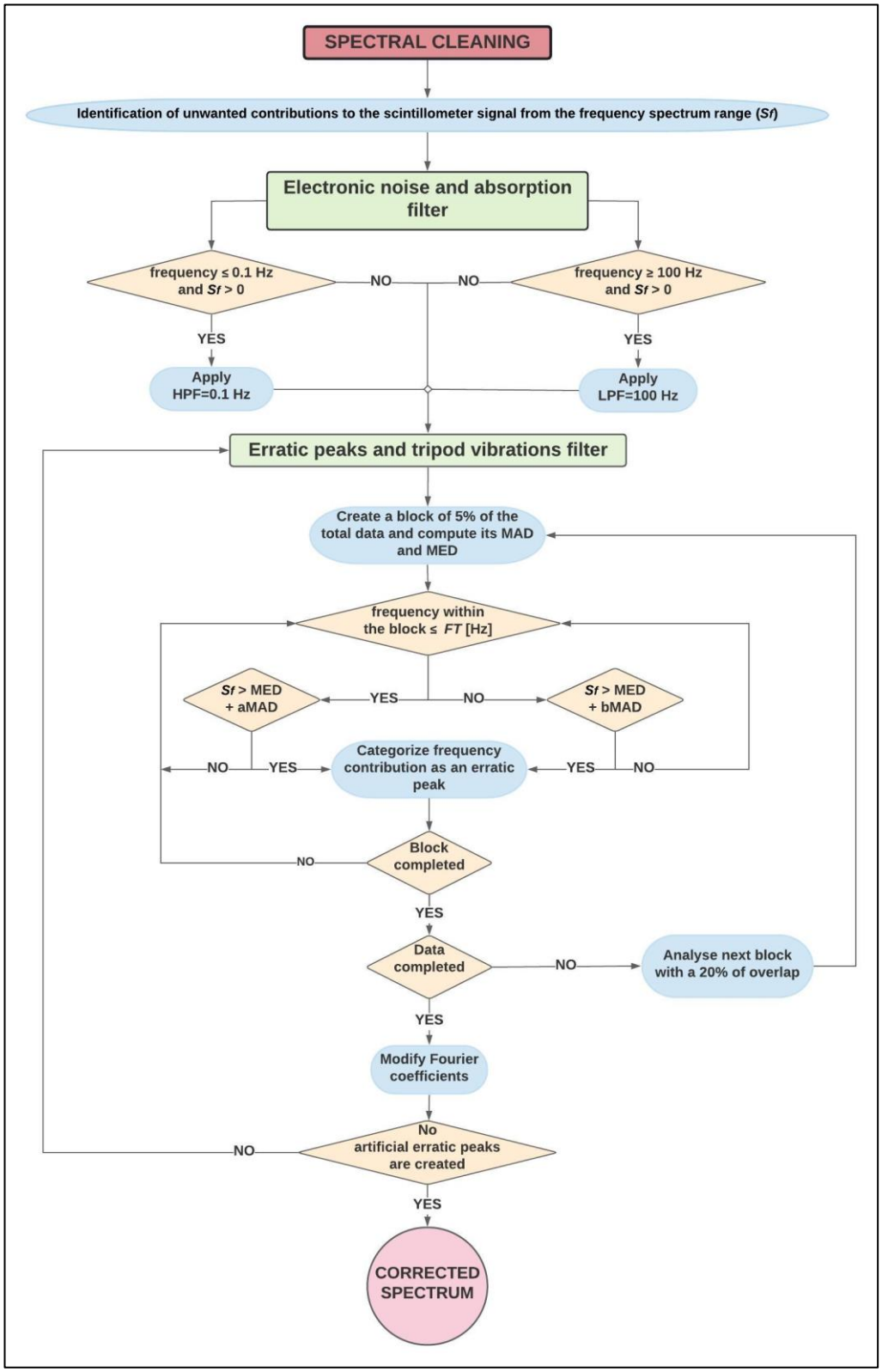

Figure 2-3: Algorithm used to filter erratic spikes and tripod vibrations contributions.

2.4 Scintillometer methods effectiveness and sensitivity of the MOST similarity functions

With the aim of analysing the effectiveness of the different theoretical methods on the estimations of H and L_vE, these results were compared to those obtained with EC. To quantify the effectiveness, an orthogonal regression was performed for each method against the EC data to derive the slope and the determination coefficient (R^2) of the best linear regression curve. Also, the energy balance ratio (EBR) was computed to analyse the EBC (Ezzahar et al., 2009):

$$EBR = \frac{\sum H + L_vE}{\sum R_n - G} \tag{19}$$

The EBR allows to evaluate the EBC by summing H and L_vE, and R_n - G over specified time periods. In this work, the integration was performed on a daily timescale.

The scintillometer theoretical method that best agreed with the EC measurements was chosen to perform a sensitivity analysis of the MOST similarity functions. For this analysis, the functions presented in Table 2-1 were used. Also, new MOST similarity functions are proposed for the conditions observed in the vineyard by iterating c_{T1} for obtaining H. Once the best agreement between H_{EC} and H_{OMS} was found, c_{q2} was modified until the best agreement between L_vE_{EC} and L_vE_{OMS} is reached.

3 Results

3.1 Original data collected by the EC and OMS

The H and L_vE measured by the EC and OMS during the field campaign are presented in Figure 3-1. Both measuring systems show that flux partitioning was slightly tilted towards H, but H and L_vE were roughly the same magnitude throughout the campaign. On one hand, the fluxes measured by the EC system are consistent with measurements performed in similar study sites with an EBR of 0.82, which has also been reported for

this type of systems (Meijninger et al., 2002; Yee et al., 2015; Foken, 2008; Mauder & Foken., 2006; Wilson et al., 2002). On the other hand, after January 10th, 2019, the scintillometer fluxes estimated with the Hill (1997) method are unrealistic as: (1) at specific times the OMS-fluxes are much larger than the solar constant (~1360 W/m^2; Li et al., 2012b); (2) the OMS-fluxes are much larger than the EC-based fluxes; (3) the OMS-fluxes are generally larger than the available energy ($R_n - G$); and (4) the large values of H and L_vE result in an EBR of 2.95, which is an extremely large value.

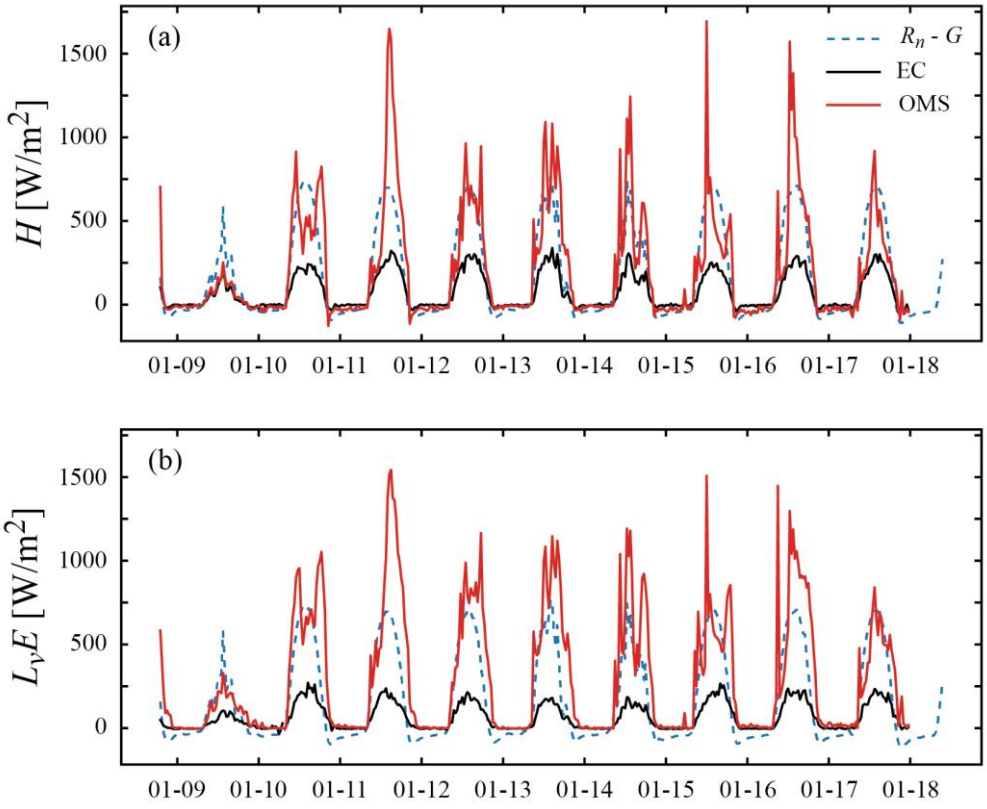

Figure 3-1: Original heat fluxes measured by the EC system and the OMS: (a) sensible heat flux (H); (b) latent heat flux (L_vE). The OMS fluxes were obtained using the Hill (1997) method. The available energy ($R_n - G$, in W/m^2) measured by the meteorological station is also shown.

From the OMS data presented in Figure 3-1 I suspect that a misalignment between the scintillometers' transmitter and receiver could have occurred on January 10th, 2019, but also wind currents possibly made the tripods unstable, as the averaged signal deviates when wind speeds reach higher values (Figure 3-2(a)). The original variances of the signals ($\sigma_{ln}^2(I)$) also present the same behaviour (Figure 3-2(b)). From January 10th, 2019, high variances are reached at the time when signal deviation due to higher wind speeds occur. Thus, averaged signal deviations and high signal variances are related. The larger signal deviation is detected during 10th, 2019. However, it coincides with an alignment process performed at 10:19 LT on January 10th, 2019, where the transmitter intensity was also increased. The same occurs at the beginning of the field campaign, where the systems were being aligned.

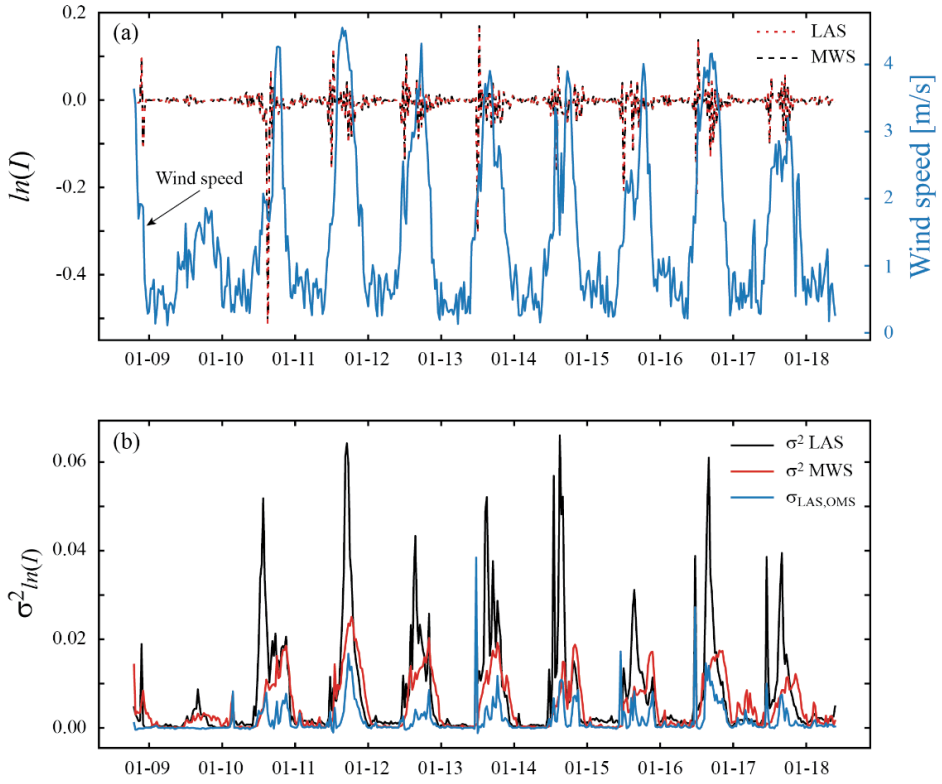

Figure 3-2: (a) Original LAS and MWS signals expressed as $ln(I)$ along with wind speed measured during the field campaign (b) Original LAS and MWS signal variances along with LAS-MWS covariance measured by the receiver during the field campaign.

There is another aspect that supports that wind is the main cause of unrealistic heat fluxes values. Even if during period January 10th, 2019 to January 18th, 2019, heat fluxes were even larger than net radiation and presented mostly unrealistic values, during the nights OMS and EC measurements agreed (Figure 3-1). During nights in Pirque wind speeds are low and, therefore, it can be argued that when higher wind speeds are reached is when EC-OMS measurements start differing. Thus, a good correlation is seen between EC and scintillometer measurements during nights until wind speeds reach higher values. Then OMS-EC measurements correlation is lost.

3.2 Identification of unwanted contributions and spectral cleaning

A spectral analysis of the data using 30-min ranges was carried out to highlight the existence of unwanted contributions. Figure 3-3 presents two examples of the data obtained during the field campaign used to illustrate the filtering procedure (Figure 2-3).

The first example is depicted in the left side of Figure 3-3. The original LAS signal, expressed as $ln(I)$, obtained on January 10th, 2019 between 13:00 and 13:30 LT is shown in Figure 3-3(a). Only the LAS signal is presented as it was the most affected signal by the wind fluctuations. Figure 3-3(b) depicts the original spectrum related to the previous signal, where interesting features are observed. First, most of the energy is located between 1 and 50 Hz. Second, electronic noise is shown as a “sawtooth”-shaped spectrum occurring at frequencies lower than 0.1 Hz. Third, spectrum peaks at ~2 Hz suggest that tripod vibrations could be occurring, as these typically have a natural frequency between 1 and 3 Hz (Ghafari et al., 2012; Pezo et al., 2016).

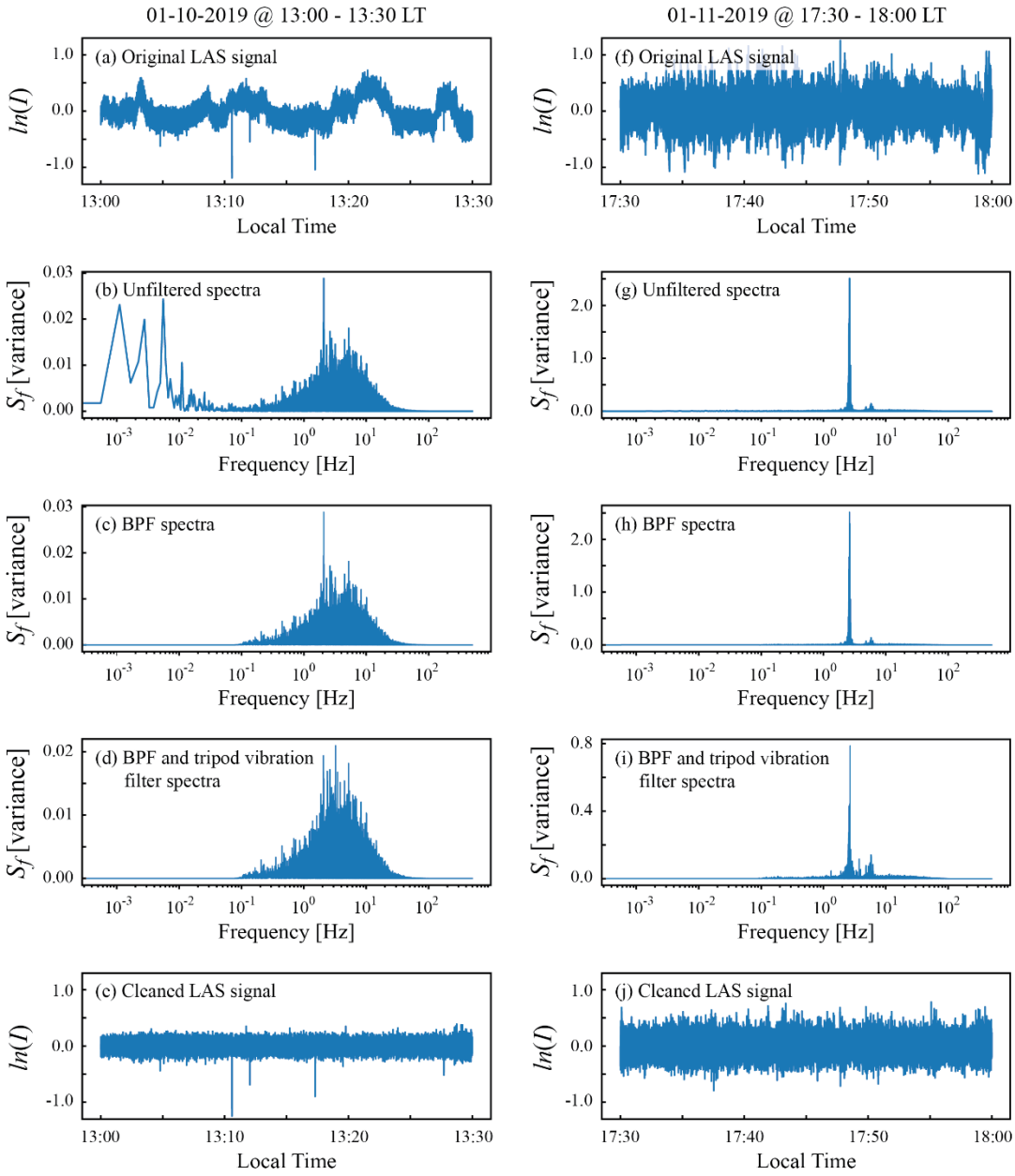

Figure 3-3: Filtering method illustrated for the LAS signal for day 2019-01-10 between 13:00 and 13:30 (left) and for day 2019-01-11 between 17:30 and 18:00 (right). (a) and (f): LAS signal expressed as *ln*(*I*). (b) and (g): original spectrum. (c) and (h): spectrum with electronic noise and absorption filter. (d) and (i) spectrum with tripod vibrations filter. (e) and (j): corrected LAS signal expressed as *ln*(*I*).

Thus, the frequency threshold (*FT*) was defined as 2 Hz. The filtered spectrum where electronic noise and absorption were removed is presented in Figure 3-3(c), in which the contributions from frequencies below 0.1 Hz and above 100 Hz are eliminated (Stoffer, 2018). The spectrum filtered with the approach proposed in this study is shown in Figure 3-3(d), where the erratic peak at ~2 Hz, which is associated to tripod variations, is eliminated. However, the erratic peak filter creates artificial peaks from the random process. Figure 3-3(e) shows the corrected LAS signal in which the mean value remains constant. In this example, the erratic spike filtering process was not as important as the electronic noise filtering process.

The second example is presented in the right side of Figure 3-3. Figure 3-3(f) shows the original LAS signal, also expressed as $ln(I)$, obtained on January 11th, 2019 between 17:30 and 18:00 LT. Figure 3-3(g) shows the original spectrum, where most of the energy is located between 2 and 7 Hz. For this case the "sawtooth"-shaped spectrum is undistinguishable as the contribution from tripod vibrations is prominent, making the spectrum reach variances of 2.5. Spectrum peaks located between 2 and 3 Hz suggests again that tripod vibrations could be occurring. Unlike the previous example, the filtered spectrum without electronic noise and absorption presented in Figure 3-3(h) does not show differences with Figure 3-3(g) as no contributions from frequencies below 0.1 Hz and above 100 Hz were detected. However, Figure 3-3(i) shows that the tripod vibrations filtering process had an impact on the spectrum, where the maximum values of the spectrum in the frequency range (i.e., the variances) are reduced from ~2.5 to ~0.8 (note the change in scale of the vertical axis). Figure 3-3(j) shows the corrected LAS signal in which the mean value remains constant. In this example, unwanted contributions from tripod vibrations are more important than electronic noise from low frequencies.

The variances obtained after applying the electronic noise and absorption filtering process, as well as the erratic peaks and tripod vibrations filter, are shown in Table 3-1. As expected, the spike filtering process of the first example was not as important as the electronic noise filtering process. In this example (left side of Figure 3-3),

variance is reduced in 84% and in 0.7% after applying the absorption and electronic noise filter, and the erratic peaks and tripod vibrations filter, respectively. For the second example (right side of Figure 3-3), variance is reduced in 21.2% and in 59.2% after applying the absorption and electronic noise filter, and the erratic peaks and tripod vibrations filter, respectively.

Table 3-1: LAS signal variances through spectral filtering for examples presented in Figure 3-3.

Example	**Original**	**Absorption and Electronic noise filter**	**Erratic spikes and tripod vibrations filter**
First (left side of Figure 3-3)	0.03736	0.00584	0.00580
Second (left side of Figure 3-3)	0.05933	0.04675	0.01907

Thus, wind speed considerably affected scintillometer heat fluxes estimations by producing unwanted contributions from tripod vibrations, but also by additional fluctuations due to misalignment that were exacerbated due to a manual increase of the transmitter intensity.

The variance and covariance of the LAS and MWS scintillometer signals were computed from the corrected signal as the area under the spectrum (Figure 3-4). This analysis helps to quantify how much of the unwanted contributions corresponds to electronic noise and absorption, and how much corresponds to high wind speeds and bad alignments. Spectral cleaning reduced unwanted contributions since variances (Figure 3-4(a) and (b)) and covariance (Figure 3-4 (c)) after applying each filter reach lower values. However, the spectral cleaning proposed in this work does not guarantee a complete signal cleaning as there are still large values of the variances observed between January 10th and 18th, 2019. For instance, the erratic spike of σ_{LAS}^2 during January 10th, 2019, which occurred due to an alignment of the scintillometers it is still

observed. Nonetheless, the signals are greatly improved. The LAS signal had more unwanted contributions than the MWS signal. On one hand, the erratic spikes and tripod vibrations filter reduces more the variances than the electronic noise and absorption filter (see LAS scintillation statistics in Figure 3-4(a)). On the other hand, electronic noise and absorption were more relevant for the MWS scintillation statistics (Figure 3-4(b)). To see the impact of the cleaning process on the time series for each scintillometer refer to Figure A.5 in Appendix C.

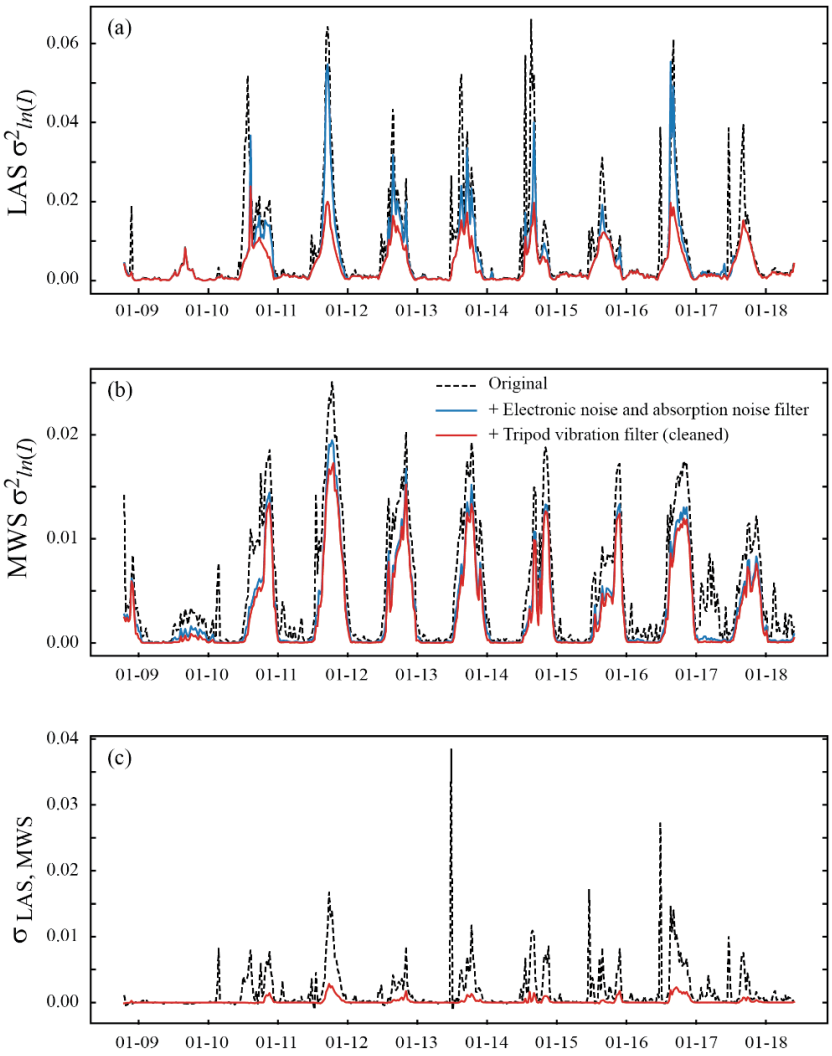

Figure 3-4: (a) Change in the variances obtained when filtering the LAS signal. (b) Change in the variances obtained when filtering the MWS signal (c) Change in the LAS-MWS signal covariance when filtering the spectrum.

Finally, from the corrected variances it was possible to recalculate OMS-based heat fluxes (Figure 3-5). Similarly than the original OMS fluxes, the corrected heat fluxes were estimated using the Hill (1997) method. Figure 3-5 and Table 3-2 show these fluxes and their comparison to the results obtained from the EC system. For the corrected fluxes, H and L_vE represent 62.3 and 79.6% of daily total R_n, respectively, and the EBR is now 1.78. Even when the corrected heat fluxes have smaller magnitudes compared to the original fluxes, the cleaning process was not enough to improve the data after the misalignment occurred (January 10th, 2019), as the fluxes are still too large, most likely due to the excessive increase in the transmitter intensity. To isolate the effect of the wind on the OMS signal without having data influenced by the misalignment and the high transmitter intensity, the effectiveness of the different theoretical methods is analysed using the data obtained on January 9th, 2019.

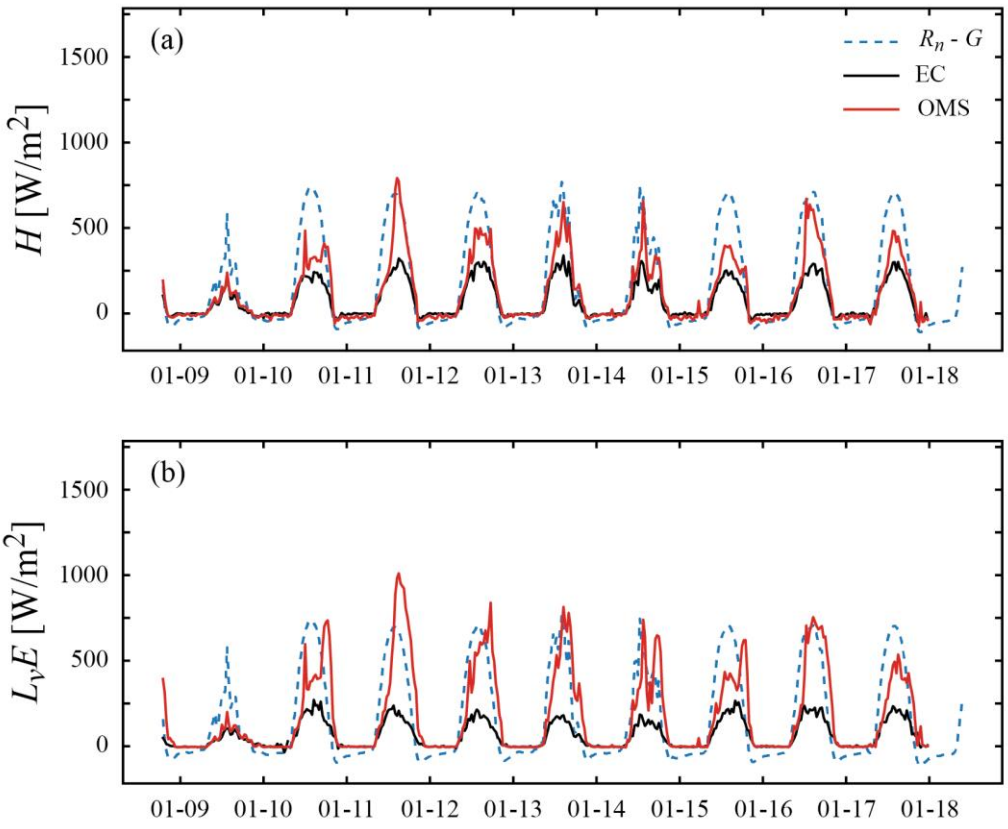

Figure 3-5: Corrected OMS fluxes after the spectral filtering process.

Table 3-2: Corrected sensible (H) and latent heat (L_vE) fluxes as a percentage of net radiation (R_n). The energy balance ratio (EBR) is also shown. Values obtained for the entire field campaign.

Method	***H* [% of daily total R_n]**	**L_vE [% of daily total R_n]**	**EBR [-]**
Eddy Covariance	35.2	29.3	0.82
Original OMS	100.5	130.9	2.95
Corrected OMS	62.3	79.6	1.78

3.3 Scintillometer methods effectiveness and sensitivity of the MOST similarity functions

Figure 3-6 presents the heat fluxes obtained by the EC on January 9th, 2019. Also, the original and corrected OMS fluxes are presented. In this case, the results of using the four theoretical methods are shown. Table 3-3 shows the heat fluxes as a percentage of R_n, as well as the EBR.

On one hand, in the EC system, G, H, and L_vE represented 11.6, 33.8 and 28.9% of the daily total R_n, respectively, with an EBR of 0.79. Total daily ET was 2.29 mm. On the other hand, the original H and L_vE OMS fluxes were 46.2 and 76.3% of the daily total R_n. Thus, daily ET was 6.07 mm, overestimating the EC results in 265%. For the corrected OMS fluxes, the results were more reasonable than those of the original fluxes obtained during the entire field campaign (compare Table 3-2 and Table 3-3). For January 9th, 2019, the corrected $H + L_vE$ never surpassed $R_n - G$, and the spectral cleaning process reduced significantly the L_vE in all the theoretical methods.

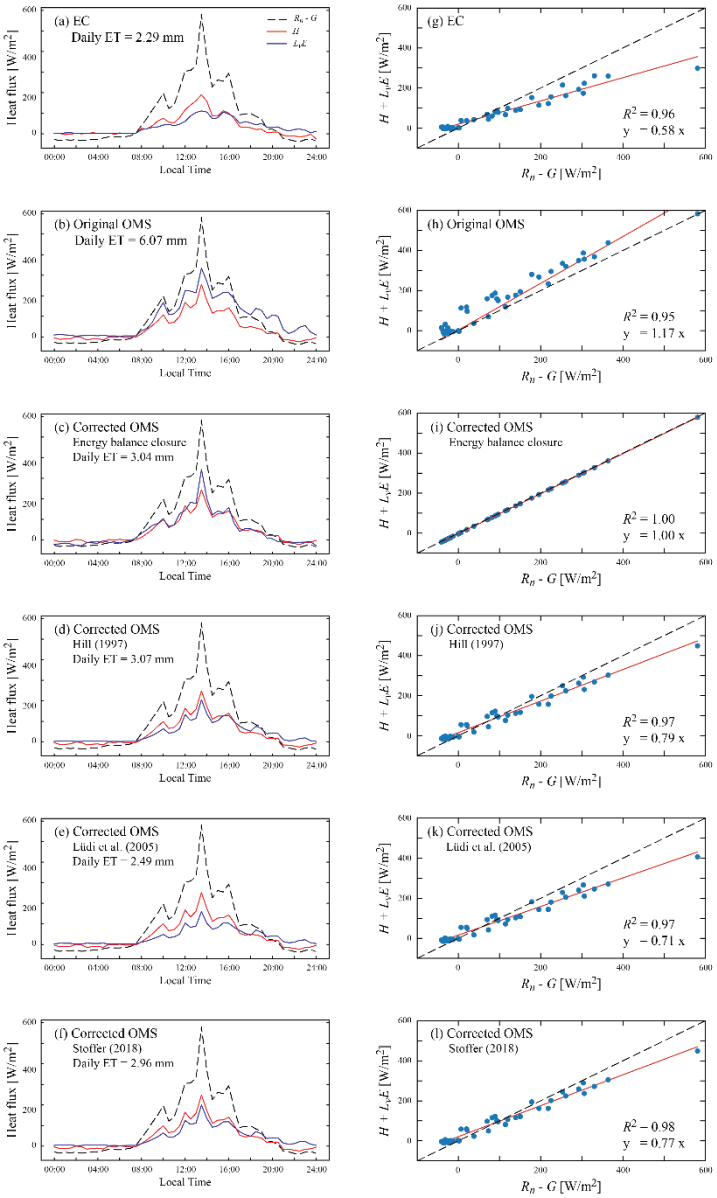

Figure 3-6: Characterization of the surface energy fluxes measured with the EC system and the scintillometers for 2019-01-09. Left: temporal daily evolution of $R_n - G$, H and L_vE measured with the EC (a) and estimated with the original OMS signal using the Hill (1997) method (b). The corrected OMS estimations were performed with the energy balance closure (c), Hill's (1997) (d), Lüdi et al. (2005) (e), and Stoffer's (2018) (f) methods. Right: energy balance closure for each of the temporal evolutions presented at the left side of the figure. The black line corresponds to the 1:1 line, the red line is the fitted line from orthogonal regression and the dots corresponds to the 30-min values of (R_n-G) and ($H + L_vE$).

Table 3-3: Sensible (H) and latent heat (L_vE) fluxes as a percentage of net radiation (R_n). The energy balance ratio (EBR) is also shown. Values obtained for January 9th, 2019.

Method	***H* [% of daily total R_n]**	**L_vE [% of daily total *Rn*]**	**EBR [-]**
EC	33.82	28.85	0.79
Original OMS	46.24	76.28	1.52
Energy Balance Closure	44.82	51.75	1.00
Hill (1997)	45.25	38.11	0.98
Lüdi et al. (2005)	46.00	31.34	0.92
Hybrid	45.46	37.21	0.97

Scatter plots comparing the EC and corrected OMS fluxes are shown in Figure 3-7. For all methods, scintillometer measurements estimated larger values of H in comparison with EC results. During the night, scintillometer methods estimate larger negative values than EC, while during the day they estimate larger positive values than EC. When H is larger than ~100 W/m^2, a larger scatter is observed. For L_vE, greater disagreement between scintillometer and EC methods is found compared to H results. This especially happens with the EBC method (Ezzahar et al., 2009), which is the one further away from EC estimations with an averaged overestimation of ~101% (Table 3-4). It presents a correlation slope of 2.08 and a determination coefficient of 0.809 (Table 3-5), which are considerably larger than those estimated with the other methods. The issue with the EBC method was expected since the EC system showed an energy imbalance with an EBR of 0.79. Thus, the EBC method yields different results than those estimated with EC. If H quantification is needed, the Hill (1997) method yields similar results to those obtained by the EC system, most likely because this method clearly recognizes the shift between day and night, so the decision of selecting a stable or unstable condition is quite clear. Regarding the other three methods, they all have the same determination coefficient (0.914; Table 3-5) and all of them estimate higher values for L_vE compared to EC during the day. During the night where stable

conditions occur, the three scintillometer methods yield very similar results to those obtained by EC, with the Lüdi et al. (2005) method being the closest to EC (overestimation of 14% of L_vE, as shown in Table 3-4). Furthermore, the Lüdi et al. (2005) method presents a correlation slope of ~ 1.07 when compared to EC (Table 3-5). For detailed results for each method refer to Figures A.6-A.9 in Appendix C.

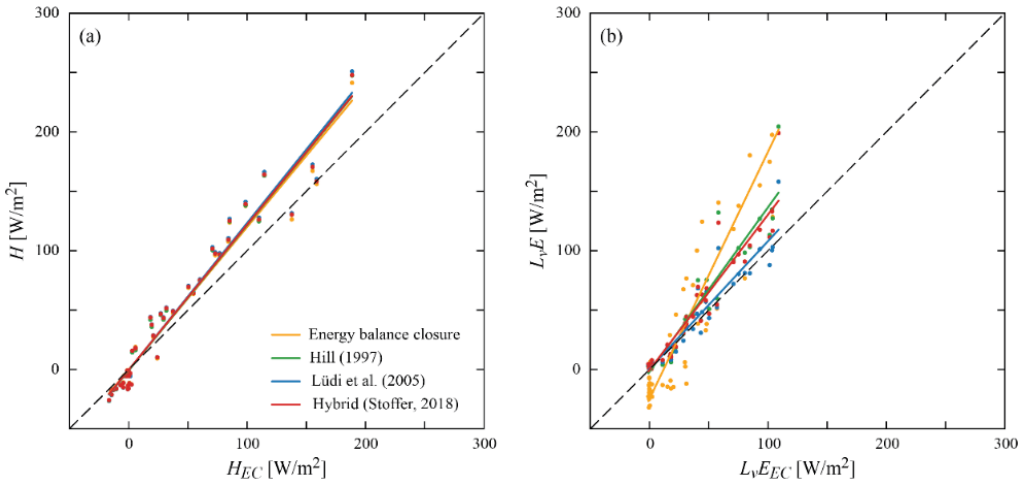

Figure 3-7: (a) Scatter plots of H (a) and L_vE (b) from the four theoretical methods in comparison with the fluxes measured by the EC system on January 9th, 2019.

Table 3-4: Overestimation (+) and underestimations (-) in comparison with the EC system.

Method	***H* [%]**	***L_vE* [%]**
Original	17.06	144.87
Energy Balance Closure	13.29	101.34
Hill (1997)	14.97	38.77
Lüdi et al. (2005)	16.72	14.29
Hybrid	15.34	34.05

Table 3-5: Correlation slopes and determination coefficient.

Method	H_{slope} [-]	H_R^2 [-]	L_vE_{slope}[%]	$L_vE_R^2$ [-]
Energy Balance Closure	1.20	0.956	2.08	0.809
Hill (1997)	1.22	0.960	1.38	0.914
Ludi et al. (2005)	1.24	0.958	1.07	0.914
Hybrid	1.23	0.958	1.31	0.914

The heat fluxes obtained with different MOST similarity functions are presented in Figure 3-8. These fluxes were estimated with the Lüdi et al. (2005) method, as this approach resembled better the EC results (see Figure 3-7, Table 3-4 and Table 3-5). The MOST similarity functions proposed coefficients for c_{T1} and c_{T2} in the field campaign are 5.5 and 15.1, and 5.6 and 1.9 for stable and unstable conditions, respectively. The proposed c_{q1} and c_{q2} coefficients are 4.5 and 1.1, and 4.5 and 9.9 for stable and unstable conditions, respectively. Table 3-6 shows how much the different similarity functions applied in the Lüdi et al. (2005) method overestimate (+) or underestimate (-) the heat fluxes compared to the EC measurements, and compared to the fluxes obtained when the Kooijmans and Hartogensis (2016) MOST similarity functions are used. For detailed results for each similarity function refer to Figure A.10 in Appendix C.

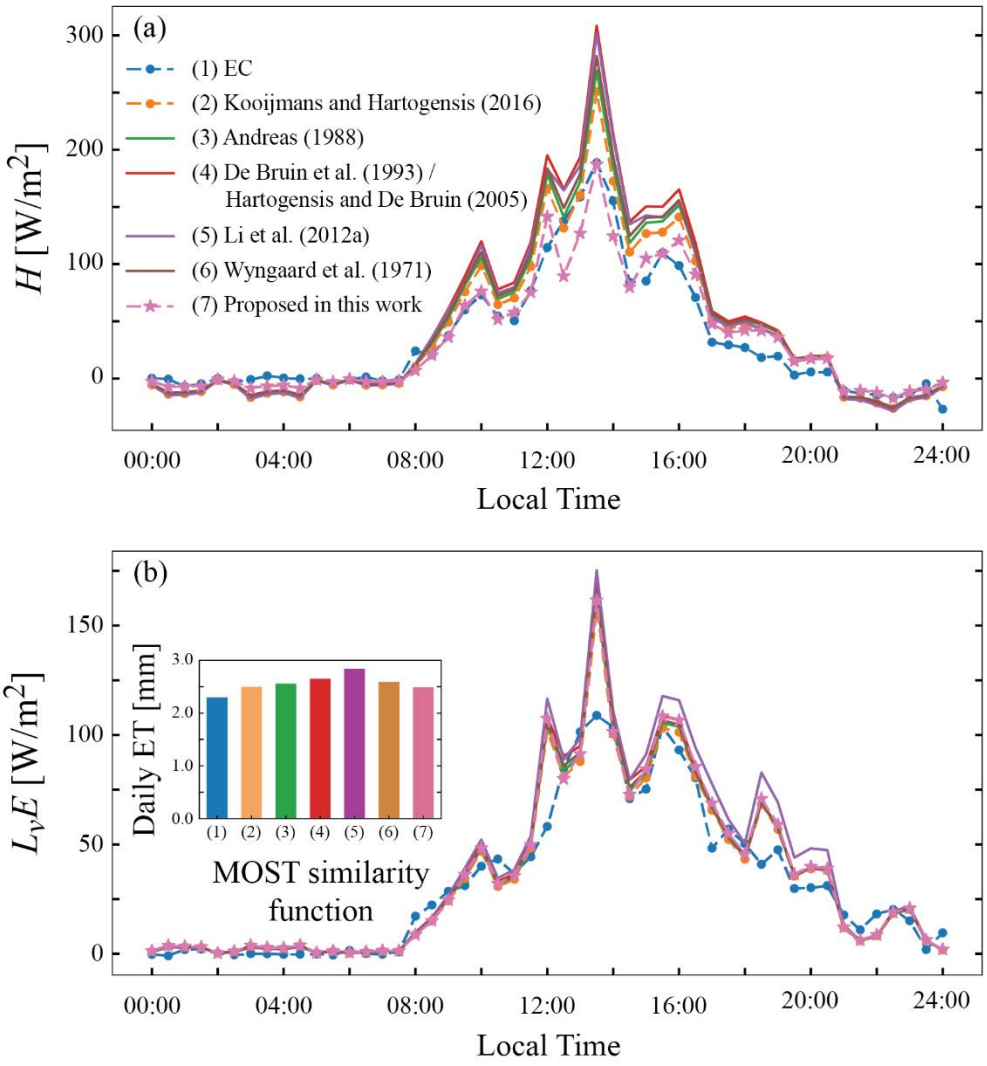

Figure 3-8: Sensible (H) (a) and latent (L_vE) (b) heat fluxes estimated using different MOST similarity functions for January 9th, 2019. The inset shows the Daily ET estimated using the different MOST similarity functions and Lüdi et al. (2005) method.

Table 3-6: Overestimation (+) and underestimations (-) of OMS heat fluxes using the Lüdi et al. (2005) method compared to EC measurements and compared to using the MOST similarity functions proposed by Kooijmans and Hartogensis (2016).

	Eddy Covariance		**Kooijmans and Hartogensis (2016)**	
Method	***H* [%]**	***L_vE* [%]**	***H* [%]**	***L_vE* [%]**
Kooijmans and Hartogensis (2016)	16.72	14.29	-	-
Andreas (1988)	25.28	17.72	7.35	2.79
De Bruin et al. (1993)	41.86	24.25	20.62	7.59
Li et al. (2012a)	37.21	27.66	15.92	12.65
Wyngaard et al. (1971)	30.61	19.86	11.60	4.36
Proposed in this work	-5.19	12.48	-20.11	-2.71

As shown in Table 3-6, the MOST similarity functions proposed by Kooijmans and Hartogensis (2016) are the ones that work better for describing the conditions observed in the vineyard. As expected, the MOST similarity functions proposed in this research agrees better when trying to represent L_vE, as this was the main aim of developing them.

4 Discussion

Scintillometer-based heat fluxes can be strongly altered when wind currents affect the measurement's physical setup. In this work, the unrealistic heat fluxes, obtained prior to reprocessing the scintillometer data, are due to deviations on the averaged signal produced when wind caused tripod vibration or scintillometer misalignment. As our spectral analysis showed unwanted contributions at different frequencies, the spectral filtering method proposed by Stoffer (2018) was used to remove unwanted contributions due to electronic noise, absorption, and erratic spikes, and extended to remove the effect of tripod vibrations, which has not been addressed before. Removing unwanted contributions from tripod vibrations is challenging as they occur in between

the optical and microwave frequencies used by scintillometers to estimate H and L_vE. Therefore, they can easily duplicate the magnitude of $\sigma_{ln}^2(f)$, strongly influencing the resulting heat fluxes. Even when the spectral cleaning method proposed in this work will not always be perfect, as it uses a probabilistic approach to remove unwanted contributions to the scintillometer signal, the corrected variances were more realistic (Figure 3-4) after filtering the data and the corrected H and L_vE agreed much better with the results obtained in the EC system (see Figure 3-1 and Figure 3-5).

In addition to performing the spectral cleaning of the raw data to remove unwanted contributions to the signal, our analysis showed that to estimate the scintillometer-based heat fluxes it is important to analyse which theoretical method and MOST similarity function are best suited for each field campaign. As most of the previous investigations available in the scientific literature deals with H measurements (De Bruin et al., 1995; Zeweldi et al., 2010; Xu et al., 2013), this analysis is crucial when estimating L_vE (and consequently ET).

On one hand, the four theoretical methods evaluated in this work agreed fairly well with the sensible heat measured by the EC system (H_{EC}), with the Hill's (1997) method achieving the best results (Figure 3-7(a)). The R^2 values related to H are higher than 0.95 for all the methods, and the correlation slope between the scintillometer-based H and the H_{EC} are between 1.20 and 1.24 (Table 3-5). These metrics agree with results presented in the literature (De Bruin et al., 1995; Meijninger et al., 2005; Zeweldi et al., 2010; Xu et al., 2013; Yee et al., 2015). On the other hand, the selection of the method for scintillometer-based L_vE (ET) estimations can lead to important differences. As shown in Figure 3-7(b), the L_vE estimated using scintillometer methods shows more dispersion when compared to L_vE measured by the EC system (L_vE_{EC}), with the Lüdi et al. (2005) and the EBC methods providing the best and worst results, respectively. Note that a worst performance of the EBC method was expected since using a standalone LAS to compute L_vE will always lead to errors when important energy imbalances are present. The R^2 values related to L_vE are ~0.91 for all the methods with the exception of the EBC that has R^2 ~0.81, and the correlation slope

between the scintillometer-based L_vE and L_vE_{EC} are between 1.07 and 1.38 (Table 3-5). Few studies comparing OMS and EC results exist in the scientific literature. Meijninger et al. (2005) found R^2 of 0.87 between L_vE estimates obtained with an OMS and an EC, with a correlation slope of 1.26, whereas Yee et al. (2015) found poor agreement for L_vE with correlation slopes ranging between 3.19 and 4.44 compared to L_vE_{EC}.

Understanding the factors that lead to differences between OMS and EC measurements is important. First, there is a footprint difference as scintillometers usually cover larger areas than EC (Foken et al., 2009). Second, EC systems cannot capture energy fluxes from larger eddies or from secondary circulations that do not touch the ground or that are stationary over the same terrain structures that generate them, i.e., bypassing the EC system (Wilson et al., 2002; Foken et al., 2009). Thus, methods that uses spatially averaging, such as scintillometers, may exhibit a tendency to close the energy balance, which was observed in the present research (Table 3-3). Third, uncertainties related to the input variables of scintillometer methods can affect the resulting scintillometer-based heat fluxes. These uncertainties depend on the spatial variation of the input variables along the scintillometer path, as well as on systematic error. According to Hartogensis et al. (2003) and Yee et al. (2015), the installation and the effective heights have a great impact on the results (Yee et al., 2015; Hartogensis et al. 2003).

Moreover, the different scintillometer theoretical methods also cause discrepancies between the estimated surface heat fluxes. These differences can be related to r_{Tq}, which can lead to inaccurate assignment of the structure parameters of temperature and humidity (Yee et al., 2015; Evans et al., 2010; Lüdi et al., 2005). For instance, using precise r_{Tq} values allowed Lüdi et al. (2005) to reach an average reduction of 13% on C_q^2, implying that L_vE fluxes are overestimated when assuming perfect correlation. Also, Wesely (1976) and Leijnse et al. (2007) demonstrated that uncertain values for r_{Tq} can cause larger errors in flux estimates for dry conditions, which was also reported by Yee et al. (2015) and Alfieri et al. (2007). For the study site, the exact computed value of r_{Tq} does not result in significant changes on the H estimation.

However, this is not the case when estimating L_vE, where the large differences in L_vE occur when the sign of r_{Tq} differs between methods during daytime. Meijninger et al. (2005) explains that C_q^2 is more sensitive than C_T^2 due to non-local effect when the fluctuations of T and q are not correlated; hence, r_{Tq} measurements have an important impact on C_q^2 (and therefore on L_vE), whereas C_T^2 shows no considerable response to r_{Tq} values. Hence, understanding the r_{Tq} behaviour is complicated. As r_{Tq} indicates the correlation between T and q fluctuations, it does not directly specify the sign of H and L_vE, rather it specifies the sign of the Bowen ratio. Thus, an additional assumption to estimate heat fluxes is needed for the scintillometer theory. Generally, L_vE is assumed to be always positive and H defines the sign of r_{Tq}. Despite this, sometimes when there is mist or dew on the surface given by water vapor in the atmosphere at night, L_vE can be slightly negative (although very close to zero). This highlights the importance of performing a spectral cleaning before obtaining the meteorological structural parameters and r_{Tq} that will be used to determine scintillometer-based H and L_vE.

MOST functions can also explain differences between the EC and OMS measurements. In this study, the similarity functions reported by Kooijmans and Hartogensis (2016) for estimating H and L_vE resulted in a good agreement between EC and OMS measurements. However, the different similarity functions used to determine L_vE resulted in large differences between the two methods. Scintillometer-based estimations were improved by proposing a new similarity function, which were based on the Kooijmans and Hartogensis (2016) MOST similarity functions. Note that the larger sensitivity of C_q^2 compared to C_T^2 described by Meijninger et al. (2005) can also be inferred by the large variability of the parameters that define the MOST similarity functions (see Table 2-1). Hence, similarity functions can yield inaccuracies, especially for L_vE (and ET) quantification. In the absence of MOST similarity functions developed for a specific site, we recommend using the functions developed by Kooijmans and Hartogensis (2016), as they are based on 11 field campaigns and have higher probabilities to function better in a study area.

5 Conclusions

This investigation demonstrates that wind currents can strongly affect scintillometer-based estimates of heat fluxes, to the point of reaching unrealistic values of H and L_vE (and consequently ET). Wind currents can alter scintillometer data through: (1) tripod vibrations, (2) misalignments due to LAS and MWS movement, and (3) electronic noise and absorption contributions to the signal. Therefore, reprocessing scintillometer data through the spectral analysis proposed in this work is an important step for computing scintillometer-based heat fluxes.

This research also found that the selection of the scintillometer theoretical method and the MOST similarity functions affects the resulting heat fluxes. On one hand, it was found that H estimations are less sensitive to the selection of the theoretical method, compared to the L_vE (and ET) estimations. The L_vE estimates are sensitive to how r_{Tq} is calculated, which explains the larger variability observed in these estimates. The Lüdi et al. L_vE estimates were closer to those obtained with the EC system, overestimating it in ~14% with a correlation slope of 1.07 and a coefficient of determination of 0.91. On the other hand, differences of ±12% in L_vE were found when using different MOST similarity functions. Our results show that the Kooijmans and Hartogensis (2016) functions are accurate for describing the study site as they were developed using data from 11 different field campaigns. Nonetheless, new proposed similarity functions yield better results for the vineyard in Pirque as they are site-specific.

As the scintillometer-based ET fluxes strongly depend on the quality of the raw data, it is strongly recommended to apply the spectral cleaning as it greatly improves scintillometer data, as well as to ensure tripod stability and correct alignment when performing scintillometer measurements. Also, it is important to understand the limitations and differences between the different theoretical methods and similarity functions used by scintillometry, as their selection has an impact on r_{Tq} values and thus on L_vE, which is relevant when quantifying ET through the scintillometer theory.

6 References

Alfieri, J., Blanken, P., Smith, D., & Morgan, J. (2007). Concerning the measurement and magnitude of heat, water vapor, and carbon dioxide exchange from a semiarid grassland. *J. Appl. Meteorol. Climatol. 48 (5), 982–996, DOI: 10.1175/2008JAMC1873.1*.

Andreas, E. (1988). Estimating c^2_n over snow and sea ice from meteorological data. *J. Opt. Soc. Amer. 5, 481–495.*

Andreas, E., Hill, R., Gosz, J., Moore, D., Otto, D., & Sarma, A. (1989). Statistics of surface-layer turbulence over terrain with metre-scale heterogeneity. *Boundary-Layer Meteorology. 86, 379–408.*

Chovanes, AE., Gochis, D., & Maxwell, R. (2020). Unraveling groundwater contributions to evapotranspiration in a mountain headwaters: Using eddy covariance to constrain water and energy fluxes in the East River Watershed. Authorea.

Culf, A., Foken, T., & Gash, J. (2013). The energy balance closure problem. in vegetation, water, humans and the climate (pp. 159-166). *Berlin: Springer Berlin.*

De Bruin, H., Kohsiek, W., & Van den Hurk, B. (1993). A verification of some methods to determine the fluxes of momentum, sensible heat and water vapour using standard deviation and structure parameter of scalar meteorological quantities. *Boundary-Layer Meteorol. 63, 231–257.*

De Bruin, H., Van den Hurk, B., & Kohsiek, W. (1995). The scintillation method tested over a dry vineyard area. *Wageningen Agricultural University, Department of Meteorology, 6701 AP, Wageningen, the Netherlands; Royal Netherlands Meteorological Institute, PO Box 201, De Bilt, the Netherlands.*

Ellsäber, F., Stiegler, C., Röll, A., June, T., Knohl, A., & Hölscher, D. (2020). Predicting evapotranspiration from drone-based thermography – a method comparison in a tropical oil palm plantation. *Biogeosciences Discuss, DOI: 10.5194/bg-2020-159.*

Ezzahar, J., Chehbouni, A., Er-Raki, S. & Hanich, L. (2009). Combining a large aperture scintillometer and estimates of available energy to derive evapotranspiration over several agricultural fields in a semi-arid region, Plant Biosystems - An

International Journal Dealing with all Aspects of Plant Biology, *143:1, 209-221, DOI: 10.1080/11263500802710036.*

Evans, J., McNeil, D., Finch, J., Murray, T., Harding, R., & Verhoef, A. (2010). Evaporation measurements at kilometre scales determined using two-wavelength scintillometry. *In: BHS Third International Symposium: Role of Hydrology inManaging Consequences of a Changing Global Environment, NewcastleUniversity, 19–23 July 2010, British Hydrological Society* http://nora.nerc.ac.uk/21124/.

Figuerola, P., & Berliner, P. (2005). Evapotranspiration under advective conditions. *International Journal of Biometeorology.*

Foken, T., Mauder, M., Liebethal, C., Wimmer, F., Beyrich, F., Leps, J., & et al. (2009). Energy balance closure for the litfass-2003 experiment. *Theoretical and Applied Climatology, 101(1-2), 149-160.*

Ghafari M., McClure G. & X. Zhang H. (2012). Assessing the variability of seismic response analysis of a tall guyed telecommunication tower with ambient vibration measurements.

Green, A., Astill, M., McAneney, K., & Nieveen, J. (2001). Path-averaged surface fluxes determined from infrared and microwave scintillometers. *Agric. Forest Meteorol. 109 (3), 233–247.*

Grimmond C. & Oke T. (1999). Aerodynamic properties of urban areas derived from analysis of surface form. J Appl Meteorol 38:1262–1292.

Hartogensis, O. (2019a). Overview of scintillometry as a method to determine land atmosphere fluxes. *Wageningen, The Netherlands.*

Hartogensis, O. (2019b). Special topics: Spectral analysis. *Wageningen, The Netherlands*.

Hartogensis, O., de Bruin, H., & Van De Wiel, B. (2002). Displaced-beam small aperture scintillometer test. part ii: Cases-99 stable boundary-layer experiment. *Boundary-Layer Meteorology, 105(1), 149-176.*

Hartogensis, O., Watts, C., Rodriguez, J., & De Bruin, H. (2003). Derivation of an effective height for scintillometers: La poza experiment in northwest mexico.

Hansen, F. (1993). Surface roughness lengths. U.S. Anny Research Laboratory AMSRL-B3E ARL-TR-61 White Sands Missile Range, NM 88002-5501.

Hill, R. (1989). Implications of monin-obukhov similarity theory for scalar quantities. *Journal of the Atmospheric Sciences*.

Hill, R. (1992). Review of optical scintillation methods of measuring the refractive-index spectrum, inner scale and surface fluxes, waves in random media. *Wave Propagation Laboratory, National Oceanic and Atmospheric Administration, Environmental Research Laboratories, 325 Broadway, Boulder, CO 80303, USA.*

Hill, R. (1997). Algorithms for obtaining atmospheric surface-layer fluxes from scintillation measurements. *NOAA/ERL Environmental Technology Laboratory, Boulder, Colorado.*

MMA-INFODEP, (2016). Elaboración de una base digital del clima comunal de Chile: línea base (1980-2010) y proyección al año 2050 INFORME FINAL. Información para el Desarrollo Productivo Ltda. (INFODEP) Estudio encargado por el Ministerio del Medio Ambiente Departamento de Cambio Climático (Coordinador Técnico: Karl-Peter Muck).

Kipp & Zonen. (2020). LAS MkII Scintillometer. Specifications. Recuperado de: https://www.kippzonen.com/Product/193/LAS-MkII-scintillometer#.X_JS0tgzY2w

Kohsiek, W., & Herben, M. (1983). Evaporation derived from optical and radio-wave scintillation. *Applied Optics, 22(17), 2566.*

Kolmogorov, A. (1941). The local structure of turbulence in incompressible viscous fluid for very large reynolds numbers. *Dokl. Akad. Nauk SSSR, 30(4): 299-303*.

Kooijmans, L., & Hartogensis, O. (2016). Surface-layer similarity functions for dissipation rate and structure parameters of temperature and humidity based on eleven field experiments.

Leijnse, H., Uijlenhoet, R., & Stricker, J. (2007). Hydrometeorological application of a microwave link: 2. Precipitation. *Water Resources Research 43 (4), DOI: 10.1029/2006WR004989*.

Lemeur, R. & Zhang, L. (1990) Evaluation of three evapotranspiration models in terms of their applicability for an arid region. Journal of Hydrology, Volume 114, Issues 3–4.

Li, D., Bou-Zeid, E., & De Bruin, H. (2012a). Monin-obukhov similarity functions for the structure parameters of temperature and humidity. *Boundary-Layer Meteorol 145:45–67*.

Li, Kejun & Feng, W. & Xu, Jingchen & Gao, Peng-Xin & Yang, L. & Hongfei, Liang & Zhan, L. (2012b). Why isn't the solar constant a constant?

Li S., Kang S., Zhang L., Zhang J., Du T., Tong T., Ding R. (2016). Evaluation of six potential evapotranspiration models for estimating crop potential and actual evapotranspiration in arid regions, Journal of Hydrology, Volume 543, Part B

Lüdi, A., Beyrich, F., & Matzler, C. (2005). Determination of the turbulent temperature-humidity correlation from scintillometric measurements.

Luque, A., García, V., Medel, F., Lillo, M., Signorio, M., Mendoza, M., Muñoz, M.C., Araya, J., de la Fuente, A., Vilà-Guerau de Arellano, J., Lobos, F., Yañez, G., Hartogensis, O., Meza, F., Suárez, F. (2019). Monitoring advection-enhanced evapotranspiration in a semiarid region irrigated field using eddy covariance and optical/microwave scintillometers. *AGU 2019 Fall Meeting. San Francisco, California, USA. December 9-13, 2019*.

Meijninger, W., Beyrich, F., Ludi, A., Kohsiek, W., & Bruin, H. (2005). Scintillometer based turbulent fluxes of¨ sensible and latent heat over a heterogeneous land surface – a contribution to litfass-2003. *Meteorology and Air Quality Group, Wageningen University and Research Centre, The Netherlands.*

Meijninger, W., Hartogensis, O., Kohsiek, W., Hoedjes, J., Zuurbier, R., & DeBruin, H. (2002). Determination of area averaged sensible heat fluxes with a large aperture scintillometer over a heterogeneous surface: Flevoland field experiment. *Boundary-Layer Meteorology 105:37–62.*

Moene, A. (2003). Effects of water vapour on the structure parameter of the refractive index for near-infrared radiation. *Wageningen University, Meteorology and Air Quality Group, Duivendaal 2, 6701 AP Wageningen, The Netherlands*.

Mohawesh O.E. (2011): Evaluation of evapotranspiration models for estimating daily reference evapotranspiration in arid and semiarid environments. Plant Soil Environ., 57: 145-152.

Monin, A., & Obukhov, A. (1954). Basic laws of turbulent mixing in the atmosphere near the ground. *Tr. Akad. Nauk SSSR Geophiz. Inst, 24(151): 163-187.*

Parasuraman, K., Elshorbagy, A. & Carey, S. (2007). Modelling the dynamics of the evapotranspiration process using genetic programming. *Hydrological Sciences Journal, 52:3, 563-578, DOI: 10.1623/hysj.52.3.563.*

Pezo M., Bakíc V. & Markovíc Z. (2016). Structural analysis of guyed mast exposed to wind action. *Laboratory for Thermal Engineering and Energy, Vinca Institute of Nuclear Sciences, University of Belgrade, Belgrade, Serbia Original scientific paper, DOI: 10.2298/TSCI16S5473P.*

RPG Radiometer Physics. (2015). Microwave Scintillometer RPG-MWSC-160. RPG Radiometer Physics GmbH Birkenmaarstr. 10 53340 Meckenheim, Germany.

Stoffer, R. (2018). Revisiting raw data processing of combined optical-microwave scintillometers. *Wageningen university and research, The Netherlands.*

van Dinther, D., Hartogensis, O., & Moene, F. (2013). Crosswinds from a single aperture scintillometer using spectral techniques. *Journal of atmospheric and oceanic technology, 30(1):3-21*.

van Kesteren, B. (2012). Measuring water-vapour and carbon-dioxide fluxes at field scales with scintillometry. *Wageningen, the Netherlands.*

van Kesteren, B., Hartogensis, O., van Dinther, D., Moene, A., de Bruin, H., & Holtslag, A. (2013). Measuring h2o and co2 fluxes at field scales with scintillometry: Part I – introduction and validation of four methods. *Agr. Forest Meteorol. 178-179:75- 87.*

Wang, T., Ochs, G., & Clifford, S. (1978). A saturation-resistant optical scintillometer to measure c2n. *JOSA, 68(3):334-338.*

Ward, H., Evans, J., Grimmond, C., & Bradford, J. (2015). Infrared and millimetre-wave scintillometry in the suburban environment - part 1: Structure parameters. *Atmospheric Measurement Techniques, 8(3):1385- 1405*.

Ward, H., Evans, J., Hartogensis, O., Moene, A., De Bruin, H., & Grimmondb, C. (2013). A critical revision of the estimation of the latent heat flux from two-wavelength scintillometry.

Wesely, M. (1976). The combined effect of temperature and humidity fluctuations on refractive index. *J. Appl. Meteorol. 15, 43–49.*

Wilson, K., Goldstein, A., Falge, E., Aubinet, M., Baldocchi, D., Berbigier, P., Bernhofer, C., Ceulemans, R., Dolman, H., Field, C., Grelle, A., Ibrom, A., Law, B., Kowalski, A., Meyers, T., Moncrieff, J., Monson, R., Oechel, W., Tenhunen, J., Verma, S. & Valentini, R. (2002). Energy balance closure at FLUXNET sites. *Agric. Forest Meteorol., 113(1-4): 223-243*.

Wyngaard, J., Izumi, Y., & Collins Jr, S. (1971). Behavior of the refractive-index-structure parameter near the ground. *J. Opt. Soc. Am. 61, 1646-1650.*

Xu, Z., Liu, S., Li, X., Shi, S., Wang, J., Zhu, Z., Xu, T., Wang, W., & Ma, M. (2013). Intercomparison of surface energy flux measurement systems used during the HiWATER-MUSOEXE. *Journal of Geophysical Research: Atmospheres. 118, 13140–13157*.

Yee, M., Pauwels, V., Daly, E., Beringer, J., Rudiger, C., McCabe, M., & Walker, J. (2015). A comparison of optical¨ and microwave scintillometers with eddy covariance derived surface heat fluxes. *Agricultural and Forest Meteorology. Australia.*

Zeweldi, D., Gebremichael, M., Wang, J., Sammis, T., Kleissl, J., & Miller, D. (2010). Intercomparison of sensible heat flux from large aperture scintillometer and eddy covariance methods: Field experiment over a homogeneous semi-arid region. *Boundary-Layer Meteorology. 135, 151–159.*

Zhang, B., Kang S., Li F., and Zhang,L. (2008). Comparison of three evapotranspiration models to Bowen ratio-energy balance method for a vineyard in an arid desert region of northwest China. *Agricultural and Forest Meteorology*, Volume 148, Issue 10.

Zhang G., Zhang J. & Meng, P. (2020). Estimation of kilometer-scale heat fluxes over a hilly area in Northern China using an optical-microwave scintillometer. *Agricultural Water Management*.

APPENDIX

APPENDIX A: EXTENDED SCINTILLOMETER THEORY

Propagation of waves in the atmosphere

Electromagnetic waves that travel through the atmosphere undergo processes of dispersion and/or absorption. In the case of scintillometers, the theory is limited to consider only the scattering processes caused by the differences in air density, ignoring the possible contribution of the scattering/absorption ratio that can occur in the path (van Kesteren, 2012).

The difference in density in the atmosphere occurs due to the presence of turbulent eddies with different humidity and temperature conditions. This is why eddies have different refractive indexes, causing them to behave like small crystals through which electromagnetic waves bend. The refractive index is then defined as the factor with which the speed of an electrodynamic wave decreases in a medium compared to vacuum. In the atmosphere the fluctuations of the refractive index are very small, and dispersion is weak. However, because eddies move both vertically and horizontally through the atmosphere, the refractive index field is constantly changing. Thus, fluctuations in the amount of scattering are generated, which are related to turbulence (van Kesteren, 2012).

Functioning of scintillometers is based on refraction and diffraction processes. When diffraction occurs, the waves are amplified in all directions and part of the emitted beam reaches the receiver in an out-of-phase manner. The concept that describes which secondary wave arrives at the receiver in phase or out of phase is known as the Fresnel zone (van Kesteren, 2012). The Fresnel zone consists of a series of ellipsoid-shaped regions that develop around the transmitter and receiver. This region is created by the diffraction of the electromagnetic signals in the air particles and its radius depends on the wavelength and the distance between the receiver and the transmitter. This allows to calculate the intensity of the wave propagation, being the first Fresnel zone that ellipsoidal space through which the direct signal passes (Leija et al., 2013). This concept is represented in Figure A.1.

The first Fresnel zone is the most important, as eddies of that size disperse more efficiently. Therefore, the first Fresnel zone must always be free of objects for the signal to reach the receiver (van Kesteren, 2012).

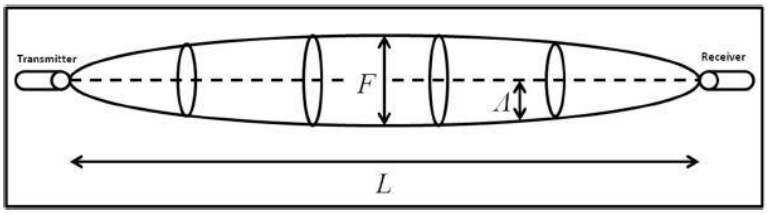

Figure A.1: Fresnel Zone, with *L* the distance between transmitter and receiver, Λ the local radius of the first Fresnel zone and *F* the maximum diameter of the first Fresnel zone (van Kesteren, 2012).

Measurement principle of a scintillometer

The functioning of a scintillometer consists of a transmitter that emits a light beam through the atmosphere to a receiver located at some distance, which records the intensity of the signal. This light beam is an electromagnetic wave with a certain wavelength that typically varies between the optical and microwave ranges. On their path length, i.e., the distance between receiver and transmitter, the light beam passes through turbulent eddies with differences in temperature, humidity, and refractive index, making the signal scatter. Thus, signal scatter is proportional to atmospheric turbulence. This scattering is detected as intensity fluctuations in the receiver (van Kesteren, 2012; Yee et al., 2015).

As the refractive index depends on temperature and humidity, each air molecule has a different refractive index. The refractive index is more sensitive to temperature changes for optical waves and sensitive to both variables in the case of microwave signals. Therefore, refractive index also depends on the wavelength (Stoffer, 2018).

Thus, the light beam is refracted on its way and the signal reaching the receiver is altered, changing the fluctuations of intensity. This happens in such a way that the greater the fluxes of sensible and latent heat in the atmosphere, the greater the difference in temperature and humidity. This implies greater refraction and fluctuations of intensity measured in the receiver. Therefore, by combining theoretical principles of atmospheric turbulence with the physics of electromagnetic wave propagation, indirectly from fluctuations measured on the receiver it is possible to obtain H and L_vE (Hill, 1989; Li et al., 2012a).

Structural parameters

The structural parameters are a measure of the turbulent energy present in the inertial range of the refractive index (Cn^2 [$m^{-2/3}$]), temperature (C_T^2 [$K^2m^{-2/3}$]), specific humidity (Cq^2 [$kg^2/kg\ m^{-2/3}$]), and temperature-humidity correlation (C_{Tq} [$kg/kg\ Km^{-2/3}$]), and depend on the specific wavelength of the light beam. Whereas structure parameters of one scalar are positive by definition (C_T^2 and C_q^2), cross-structure parameters like C_{Tq} may be negative (Wang et al., 1978).

As an example, the refractive index structural parameter C_n^2 can be defined as:

$$C_n^2 = \frac{\overline{[n(r_1)-n(r_2)]^2}}{r_{12}^{2/3}} \qquad \text{(A.1)}$$

where r_1 and r_2 are two points in space separated by a distance r_{12}, and n is the index of refraction at that point in space.

According to Wang et al. (1978), scintillations produced by turbulence near the centre of the transect contributes more to the path averaged C_n^2 than the ones produced closer to the transmitter and receiver. This means that C_n^2 is path averaged according to a spatial bell-shaped weighting function (Bruin et al., 1995).

Since structural parameters measure the turbulent energy present in the inertial range, they can quantify the turbulence causing scintillations in the atmosphere (Wang et al., 1978). In the inertial range is where optical and microwave scintillometers are more sensitive and is where the spectrum is directly proportional to the structural parameter. This leads to the deduction that the structural parameters are proportional to the total amount of turbulent energy (Stoffer, 2018). Thus, from the information of the temperature field described by the temperature structural parameter (C_T^2) scintillometers can estimate the surface fluxes of the turbulent fields, specifically sensible heat.

The temperature spectrum in the sub-inertial range is known as the Kolmogorov spectrum and is defined through the one-dimensional wave number (k) (Kolmogorov, 1941).

$$\phi_T(k) = 0.1245 \cdot C_T^2 \cdot k^{-\frac{5}{3}} \tag{A.2}$$

which is also valid for estimating humidity. With this, structural parameter of temperature C_T^2 and structure parameter of humidity C_q^2, can be estimated from a point sensor. However, in order to obtain C_T^2, C_q^2 and C_{Tq} it is necessary to have a complete quantification of the atmospheric temperature spectrum, or in other words, a precise description of the refractive index spectrum. The three-dimensional turbulent spectrum of the refractive index is defined by Kolmogorov (1941) as:

$$\phi_n(K) = 0.033 C_{n,\lambda}^2 K^{-\frac{11}{3}} \tag{A.3}$$

where K is the three-dimensional wavenumber.

Types of scintillometers

1. Large aperture scintillometer (LAS)

This type of scintillometer operates on wavelengths close to infrared. In this range temperature fluctuations given by C_T^2 are the main cause of the oscillation of optical wavelengths. Therefore, optical scintillometers allow the calculation of H without making measurements or assumptions about humidity fluctuations (Yee et al., 2015). Then, with structural parameters, wind speeds and relative humidity sensible heat can be estimated. However, this type of scintillometer do not estimate latent heat flux directly. Thus, energy balance closure is used to be able to calculate $L_v E$ after sensible heat fluxes has been estimated.

In order to compute energy balance is necessary to model the interaction between the atmosphere, vegetation and land through the following two equations (Braam & Vila-Guerau de Arellano, 2019):

i. Radiation balance: energy entering the surface.

It consists of the input and output of radiation of short wavelengths and long wavelengths. Short wave radiation is the direct radiation from the sun, which depends on the location on earth, the day, the hour and the amount of clouds. Its output depends on the reflection conditions of the surface and the albedo. In the case of long-wave radiation, it is based on Boltzmann's law and its input depends on the boundary layer while its output depends on the surface temperature.

ii. Energy balance: the energy that goes in equals the energy that comes out.

The distribution of energy at the surface consists of the sensible heat (H) responsible for heating the boundary layer, the ground heat (G) responsible for heating the soil and the rest is latent heat (L_vE) for evaporating water from the soil

and vegetation. All of them are vertical fluxes, but advection processes which are horizontal can also alter the balance. Figure A.2 shows each component.

The overall energy balance equation in its most simple form is written as (Culf et al., 2013):

$$R_n - G = H + L_v E \tag{A.4}$$

where L_vE is the evapotranspiration written in terms of energy fluxes. As a convention, it is considered that radiative fluxes are positive downwards, while the others are considered positive upwards when directed away from the surface. This energy balance is used to model the interaction between the soil and the atmosphere, and to evaluate the accuracy of estimates of EC fluxes in terms of net radiation (R_n).

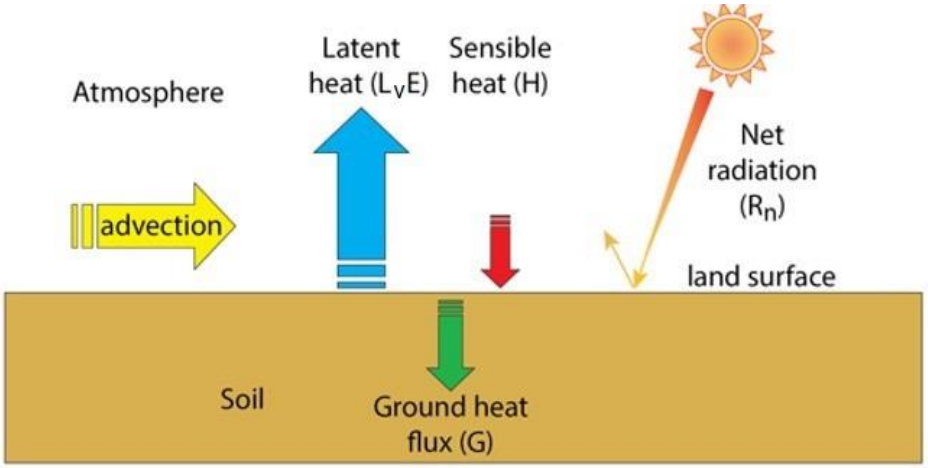

Figure A.2: energy balance scheme.

Going a little deeper into each of the terms, sensible heat depends on the temperature gradient, with aerodynamics being an important aspect to consider. Related to latent heat, the magnitude of the flux depends on the presence of vegetation, the state of the land and the presence of liquid water in the soil or vegetation. Thus, L_vE depends on the amount of humidity (q) existing. Surface heat is calculated from the saturation specific humidity (q_{sat}), which depends on the surface temperature. Thus, humidity is

related to the rate of transformation of water from the earth to the atmosphere and depends on both its properties, such as water content and the properties of vegetation (Braam & Vila-Guerau de Arellano, 2019).

The distribution of energy depends on the characteristics of the atmosphere and the soil. For semi-arid and arid regions sensible heat is expected to be greater than latent heat flux, since there is not enough vegetation to require energy for evapotranspiration. This is measured by Bowen number (β), which is defined as H/L_vE. Then, for semi-arid regions β is expected to be larger than 1, or at least 1.

However, it has been shown since the 1980s that Earth's surface energy balance cannot be closed with experimental data. The sum of net radiation and the ground heat flux has been found to be larger than the sum of turbulent fluxes of sensible and latent heat in most cases (Foken & Oncley, 1995). The complete energy balance equation can be written as (Wilson et al., 2002):

$$L_vE + H = R_n - G - S - Q \tag{A.5}$$

where the new components are the rate of change of heat storage (S) between the soil surface and the level of the instrumentation, and the sum of all additional sources and sinks (Q). Imbalances in energy closure can be given by (Culf et al., 2013; Foken et al., 2006; Wilson et al., 2002):

(a) Sampling errors associated with different measurement source areas

(b) Systematic bias in instrumentation

(c) Neglected energy sinks or advection

(d) Loss of low and/or high frequency contributions to the turbulent flux

(e) Incomplete understanding of physics

(f) Inability to measure or calculate each term

Typical energy balance closure residual during the day has been found as 50-300 W/m^2 and for agricultural fields an average of 20-30% (Foken, 2008; Mauder & Foken., 2006; Wilson et al., 2002). This is characterized by underestimations of sensible and latent heat flux or overestimations of net radiation and ground heat flux, presence of advection and also by the necessary energy for photosynthesis as a storage problem (Foken, 2008). Also, it has been found that measuring height of turbulent fluxes has a significant influence on the footprint and heat storage that affects the closure. Also soil heterogeneity can considerably affect the results (Liebethal et al., 2005).

2. Microwave scintillometer (MWS)

This scintillometer operates at microwave lengths and is sensitive to both humidity and temperature fluctuations. Hence, by combining a LAS and MWS scintillometer heat fluxes can be obtained without using energy balance closure as a method to obtain L_vE (Ezzahar et al., 2009). The combination of these two scintillometers, a LAS operating at optical wavelength and a MWS operating at microwave length, is known as Optical Microwave Scintillometer (OMS).

Both devices operate simultaneously on the same path, where the LAS is just sensitive to temperature and the MWS is sensitive to both temperature and humidity fluctuations. Thus, there are two structural parameters of refractive index associated to each wavelength. Then, in order to obtain the structural parameters, one more equation is needed.

Scintillometer measurements: from waves in the atmosphere to $\sigma_{ln^2(I)}$

Quantifying wave scattering in a turbulent atmosphere is complex and requires multiple techniques and simplifications in order to solve the equation that describes its behaviour.

The starting point is Maxwell's equations, with which through the use of different assumptions the solution of the equation of an electromagnetic wave dispersed by atmospheric turbulence can be found (van Kesteren, 2012). This solution is based on the logarithm of the amplitude A of the wave, which is denoted as $\chi' 2 = ln(A)$.

The solution of the equation of an electromagnetic wave dispersed by atmospheric turbulence is:

$$\overline{\chi'^2} = 4\pi^2 k^2 \int_0^L \int_0^\infty k\phi_n\,(k, C_n^2, l_0) sin^2\left(\frac{k^2 x(L-x)}{2kL}\right) dxdk \qquad (A.6)$$

where k is the eddy wave number, x the position within the path between receiver and transmitter of length L, ϕ_n is the refractive index spectrum defined by equation (A.3), Cn^2 the structural parameter of refractive index and l_0 the limit value defining the transition between the inertial and dissipation sub-range.

However, the detector in the scintillometer does not measure the amplitude of the wave. It measures the intensity I of the propagated wave and returns a voltage such that the signal intensity is equal to the measured intensity. As $I = A^2$, the variance of the logarithmic intensity of the wave equals 4 times the variance of its logarithmic amplitude (Lawrence & Strohbehn, 1970):

$$\overline{(\ln(I)')^2} = \overline{4\chi'^2} \qquad (A.7)$$

Ideally, only dispersion is considered to induce variance in $ln(I)$. However, in reality there are contributions associated with absorption and electronic noise that induce additional variance. For this purpose, filter pass bands are used to eliminate high and low frequencies of noise and absorption (Stoffer, 2018; Van Kesteren, 2012).

It is not evident how the spatial distribution of the eddies influences the variance, because not all eddies in a certain position of the path contribute to fluctuations in intensity. Smaller eddies, i.e. those with a greater number of waves, cause less fluctuations in intensity when compared to larger eddies given the same position and eddies at the centre of the path cause greater fluctuations in signal strength compared to the edges, i.e. positions close to the receiver and transmitter. According to van Kesteren (2012), to have the same contribution to the fluctuations at the edges as in the centre, the edges need larger wavenumber eddies. This is due to the existence of the Fresnel zone, since when normalized by 2Λ the curvature disappears. Thus, the contribution of an eddy depends on the relationship between its dimension and the one from the first Fresnel zone.

Writing the general solution of the wave equation for intensity as a function of the radius of the first Fresnel zone (Λ) and the wavelength of the eddy $\left(\lambda = \frac{2\pi}{k}\right)$ gives the following equation:

$$\overline{(\ln(I)')^2} = \pi^2 k^2 \int_0^L \int_0^\infty k\phi_n\,(k, C_n^2, l_0) sin^2\left(\pi \frac{\Lambda^2}{\lambda^2}\right) dxdk \qquad (A.8)$$

This gives a trajectory weighting function and an eddy weighting function for one point and two scintillometers, which has shown that the scintillometer is more sensitive in the centre of the trajectory than at the edges. This defines what is known as a ‘footprint’ which refers to the contribution of each area to the measurements of turbulent flux, being fundamental for heterogeneous places. According to van Kesteren (2012), the footprint depends on various factors, including the height above ground at which the scintillometer is located, the stability of the scintillometer, the wind speed and the wind direction.

Wave equation: from $\sigma_{ln^2(I)}$ to C_n^2

The previous section showed that the contribution to intensity fluctuations $\overline{(\ln(I)')^2}$, from now on $\sigma^2_{\ln(I)}$, is the result of the integration of turbulence and wave propagation properties over scales of turbulence measured as a function of the wave number *k* and the path *x* between the receiver and the transmitter. If this equation is solved, the structural parameter of refractive index can be obtained.

Assuming a Kolmogorov spectrum the solution is reduced to:

$$\sigma^2_{\ln(I)} = 0.13 C_n^2 k^{\frac{7}{6}} L^{\frac{11}{6}} \quad if \quad \sqrt{\lambda L} \gg l_0 \tag{A.9}$$

$$\sigma^2_{\ln(I)} = 0.246 C_n^2 L^3 l_0^{-7/3} \quad if \quad \sqrt{\lambda L} \ll l_0 \tag{A.10}$$

According to Wang et al. (1978), the analytical solutions that relate $\sigma_{ln^2(I)}$ and C_n^2 for different wavelengths (λ_{opt} and λ_{mw} for the optical and microwave range, respectively) can be written as:

$$\sigma^2_{\ln(I),opt} = c_{opt} D^{\frac{-7}{3}} L^3 C^2_{n,opt} \tag{A.11}$$

$$\sigma^2_{\ln(I),mw} = c_{mw} F^{\frac{-7}{3}} L^3 C^2_{n,mw} \tag{A.12}$$

$$\sigma^2_{\ln(I),opt,mw} = c_{opt,mw} max(D,F)^{\frac{-7}{3}} L^3 C^2_{n,opt,mw} \tag{A.13}$$

in which c_{opt}, c_{mw} and $c_{opt,mw}$ are constants [-] where the subindices *opt*, *mw* and *opt,mw* refer to optical, microwave, and optical-microwave, *L* is the path length [m], *D* is the optical scintillometer diameter [m] and $F = \sqrt{\lambda L}$ is the Fresnel length [m].

Wave equation: from C_n^2 to C_T^2, C_q^2 and C_{Tq}

Thus, it can be seen that from intensity fluctuations $\sigma_{ln^2(I)}$ measured in the receiver C_n^2 can be estimated. However, heat fluxes are not directly related to C_n^2 but to the temperature structural parameter C_T^2 for estimating *H*, and to the humidity structural

parameter C_q^2 for estimating L_vE. Hill (1997) derived empirical formulas that relate the C_n^2 to the structural parameters C_T^2, C_q^2 and C_{Tq} by applying the Reynolds' decomposition:

$$C_n^2 = \frac{A_T^2}{\bar{T}^2} C_T^2 + \frac{2A_T A_q}{\overline{T_q}} C_{T_q} + \frac{A_q^2}{\bar{q}^2} C_q^2 \tag{A.14}$$

where T is temperature [K], q is specific humidity [kg/kg], and A_i are dimensionless coefficients [-] dependent on atmospheric pressure, temperature and specific humidity. Overbars denote mean values over a temporal interval. In equation (A.14), C_T^2, C_q^2, and C_{Tq} are independent of the light beam wavelength, while the rest are dependent of it.

The non-dimensional coefficients are dependent on meteorological data described by Ward et al. (2013):

$$A_t = -\frac{\bar{P}}{\bar{T}}\left(b_{t1} + b_{t2}\frac{R_v}{\bar{R}}\bar{q}\right) \tag{A.15}$$

$$A_q = -\frac{\bar{P}}{\bar{T}}\frac{R_v}{\bar{R}}\bar{q}b_{q2}\left(1 - \frac{\bar{q}}{\bar{R}}(R_v - R_d)\right) \tag{A.16}$$

For optical scintillometers:

$$b_{t1} = \left(0.237134 + \frac{68.39397}{130-\lambda^{-2}} + \frac{0.45473}{38.9-\lambda^{-2}}\right)\cdot 10^{-6} \tag{A.17}$$

$$b_{t2} = b_{q2} = (0.648731 + 0.0058058\lambda^{-2} - 0.000071150\lambda^{-4} + 0.000008851\lambda^{-6})\cdot 10^{-6} - b_{t1} \tag{A.18}$$

and for millimetre-wave scintillometer:

$$b_{t1} = 0.776\cdot 10^{-6} \tag{A.19}$$

$$b_{t2} = \left(\frac{7500}{\bar{T}} - 0.056\right)\cdot 10^{-6} \tag{A.20}$$

$$b_{q2} = \left(\frac{3750}{\bar{T}} - 0.056\right) \cdot 10^{-6} \quad \text{(A.21)}$$

Green et al. (2001) found that the LAS is sensitive to temperature fluctuations and therefore to C_T^2, while the MWS is sensitive to both temperature and humidity fluctuations, but more sensitive to C_q^2. In both cases C_{Tq} is not negligible. Since LAS is more sensitive to C_T^2 and little information is usually available on C_{Tq} and C_q, additional information on the relationship between T and q fluctuations is used when using a standalone LAS (Wesely, 1976). For this, Moene (2003) added a correction to the effect of C_q and C_{Tq} over C_n^2, known as the Bowen's correction, which assumes that the correlation coefficient between the temperature and humidity fluctuations (r_{Tq} [-]) is ±1:

$$C_n^2 = \frac{A_T^2}{\bar{T}^2} C_T^2 \left(1 + \frac{A_q}{\bar{q}} \frac{\bar{T}}{A_T} \frac{c_p}{L_v} \beta^{-1}\right)^2 \quad \text{(A.22)}$$

where β is the Bowen ratio and c_p the specific heat at constant pressure. In case of using OMS scintillometers, there are two equations for $C_n^2{}_{opt}$ and $C_n^2{}_{mw}$, and three unknowns. In view of this, three approaches are proposed to solve the equations and obtain the desired structural parameters.

i. Hill's (1997) two-wavelength method

It consists of assuming that the three structural parameters are not independent, and that the r_{Tq}, defined in equation (A.23), is ± 1 (positive for the unstable conditions that occur during day and negative for the stable conditions that occur during night):

$$r_{Tq} = \frac{C_{Tq}}{\sqrt{C_T^2 C_q^2}} \quad \text{(A.23)}$$

Many investigations have used the two-wavelength method (Andreas et al., 1989; Green et al., 2001; Kohsiek and Herben, 1983; Meijninger et al., 2002). However, for non-ideal flows, assuming r_{Tq} = ±1 is not always valid, especially over heterogeneous

terrain (Lüdi et al., 2005) as the MOST assumptions are infringed. For this reason, Lüdi et al. (2005) proposed using 0.8 for day and -0.6 for night when using Hill's (1997) method.

Using this approach, solutions for equation (A.14) give values for C_T^2 , C_q^2 and C_{Tq} (Stoffer, 2018):

$$C_T^2 = \left[Aq_{mw}^2 C_{n,opt}^2 + Aq_{opt}^2 C_{n,mw}^2 + 2Aq_{opt}^2 Aq_{mw}^2 r_{Tq}\sqrt{C_{n,opt}^2 C_{n,mw}^2}\right]\frac{T^2}{\gamma^2} \quad \text{(A.24)}$$

$$C_q^2 = \left[At_{mw}^2 C_{n,opt}^2 + At_{opt}^2 C_{n,mw}^2 + 2At_{opt}^2 At_{mw}^2 r_{Tq}\sqrt{C_{n,opt}^2 C_{n,mw}^2}\right]\frac{q^2}{\gamma^2} \quad \text{(A.25)}$$

$$C_{Tq} = r_{Tq}\sqrt{C_T^2 C_q^2} \quad \text{(A.26)}$$

where $\gamma = At_{mw}^2 Aq_{opt}^2 - At_{opt}^2 Aq_{mw}^2$.

ii. Lüdi et al. (2005) bichromatic method

This method is based on the covariance between the signals from optical and microwave scintillometers to derive structural parameter C_{Tq}. The path-averaged C_{Tq} is found by cross-correlating the two electromagnetics signals at different wavelengths that pass through the same air volume (Lüdi et al., 2005). This approach has the advantage that no assumptions are made to find C_{Tq}. However, the bichromatic approach is less robust than the two-wavelength method as sometimes it delivers chaotic behaviour or unrealistic r_{Tq} values (Lüdi et al. 2005; Stoffer, 2018).

Using this approach, solutions for equation (A.14) gives values for C_T^2 , C_q^2 and C_{Tq} (Stoffer, 2018):

$$C_T^2 = \left[Aq_{mw}^2 C_{n,opt}^2 + Aq_{opt}^2 C_{n,mw}^2 - 2Aq_{opt}^2 Aq_{mw}^2 C_{n,opt,mw}\right]\frac{T^2}{\gamma^2} \quad \text{(A.27)}$$

$$C_q^2 = \left[At_{mw}^2 C_{n,opt}^2 + At_{opt}^2 C_{n,mw}^2 - 2At_{opt}^2 At_{mw}^2 C_{n,opt,mw}\right]\frac{q^2}{\gamma^2} \quad \text{(A.28)}$$

$$C_{Tq} = \left[-At_{mw}Aq_{mw}C_{n,opt}^2 - At_{op}Aq_{op}C_{n,mw}^2 + \left(At_{opt}Aq_{mw} + Aq_{opt}At_{mw}\right)C_{n,opt,mw}\right]\frac{Tq}{\gamma^2} \quad \text{(A.29)}$$

iii. Stoffer's (2018) hybrid method

The most recent approach to find the structural parameters, also known as the hybrid method, was developed by Stoffer (2018). This approach uses corrected r_{Tq} values estimated from the Lüdi et al. (2005) method, and applies them in the Hill (1997) method to compute heat fluxes. This procedure reduces the chaotic behaviour of the r_{Tq} values obtained from the Lüdi et al. (2005) method, and it produces more robust results than those obtained in the Hill (1997) method (Stoffer, 2018).

Therefore, solving for C_T^2, C_q^2 and C_{Tq} Lüdi et al. (2005) equations (A.27), (A.28) and (A.29), temperature - humidity correlation can be computed by using equation (A.23). Then, a whole cleaning process is done and cleaned r_{Tq} values are used in equations (A.24), (A.25) and (A.26) to obtain Hill (1997) C_T^2, C_q^2 and C_{Tq}.

Stoffer (2018) hybrid method cleaning process consists on first removing unrealistic values where $r_{Tq} > |1|$ by setting values between 1 and 4 to 0.8, and between -1 and -4 to -0.6. Values above 4 are completely removed. Then erratic sign-changes are removed, which are r_{Tq} surrounding two intervals with both an opposite sign. The erratic sign-change value is replaced by the r_{Tq} value of the preceding interval and a smooth process is done by applying a moving average with a window size equal to 5 intervals. The resulting r_{Tq} values are used to prescribe r_{Tq} in Hill (1997) method.

Another interesting thing of the method is that a quality flag is applied, which indicates how reliable the sign of r_{Tq} is after the cleaning process. The score varies between 0 for very unreliable values and 1 for very reliable ones.

The flag is calculated as:

$$flag = |rTq| \cdot \left(1 - \overline{std(r_{Tq})}\right) \tag{A.30}$$

where $std(r_{Tq})$ indicates a moving average of the standard deviation over 10-minute intervals. The threshold was defined as 0.3 to decide whether the sign of r_{Tq} is reliable or not. For all intervals where the score is lower than 0.3, the sign is classified as unreliable.

Monin-Obukhov similarity theory: from structural parameters to *H* and L_vE

Structural parameters C_T^2 and C_q^2 can be directly related to sensible heat and latent heat flux, respectively, through Monin-Obukhov similarity theory (MOST). MOST is used to describe turbulence characteristics in the atmospheric surface layer, allowing to relate measured turbulence statistics to temperature, humidity and wind scales. These magnitudes are defined in terms of the turbulent fluxes of heat (H), moisture (L_vE), momentum (τ). Therefore, with the help of the just presented theoretical principles of atmospheric turbulence and the understanding of electromagnetic wave propagation, surface heat fluxes can be obtained (Van Kesteren, 2012). According to Monin and Obukhov (1954) similarity theory C_T^2 and C_q^2 scale with $\theta_*^2/(z-d)^{2/3}$ and $q_*^2/(z-d)^{2/3}$, respectively, through the MOST universal similarity functions $f_{C_T^2}$ and $f_{C_q^2}$:

$$\frac{C_T^2(z-d)^{2/3}}{\theta_*^2} = f_{C_T^2}\left(\frac{z-d}{L_O}\right) \tag{A.31}$$

$$\frac{C_q^2(z-d)^{2/3}}{q_*^2} = f_{C_q^2}\left(\frac{z-d}{L_o}\right) \tag{A.32}$$

with L_o [m] the Obukhov length, z is the beam effective height [m], d the zero-plane displacement, θ_* the temperature turbulent scale [K] and q_* the humidity turbulent scale [kg/kg]. The 'Obukhov length' represents the height above the surface where friction and convective turbulence production are equal. It can be estimated as:

$$L_O = -\frac{T}{kg}\frac{u_*^2}{\theta_*} \tag{A.33}$$

with T temperature [K], κ is the von Kármán constant (0.4), g is gravity (9.8 m/s^2) and u_* is the friction velocity [m/s]. However, scintillometers type (LAS/MWS) do not contain information about friction velocity, so flux-profile-relationships must be used. Therefore, u^* can be estimated by the standard Businger-Dyer flux-profile relation (Stull, 1988):

$$u_* = \frac{k[\bar{u}(z_2-d)-\bar{u}(z_1-d)]}{\ln\left(\frac{z_1-d}{z_2-d}\right)-\Psi\left(\frac{z_1-d}{L_O}\right)+\Psi\left(\frac{z_2-d}{L_O}\right)} \tag{A.34}$$

were $\bar{u}$ [m/s] is the mean wind speed at height z [m], d the zero-plane displacement [m] and Ψ is a function dependent on z/L_O, which represents the stability of the atmosphere.

What is usually done to estimate u_* is using the roughness length were wind speed is zero, so just one value for u is needed. The roughness length and the zero-plane displacement represent the effect in the intensity of mechanical turbulence and fluxes measurement by the surface irregularity. For unstable atmospheric conditions ($z/L_O <$ 0):

$$\Psi\left(\frac{z-d}{L_O}\right) = 2\cdot\ln\left(\frac{1+x}{2}\right)+\ln\left(\frac{1+x^2}{2}\right)-2\cdot arctan(x)+\frac{\pi}{2} \tag{A.35}$$

$$x = \left(1-16\frac{z-d}{L_O}\right)^{1/4} \tag{A.36}$$

For stable conditions, Duynkerke et.al (1999) approximation can be used:

$$\Psi\left(\frac{z-d}{L_O}\right) = 1-\left(1+\frac{d}{e}\cdot\frac{z}{L_O}\right)^e \tag{A.37}$$

with e=0.8 and d=0.5. When heat fluxes are closer to zero, a correction was found by applying instead:

$$\Psi\left(\frac{z-d}{L_O}\right) = 1 - \left(1 + \frac{d}{e} \cdot \frac{z}{L_O}\right)^{e-1} \tag{A.38}$$

Then, it can be seen that L_o and $u*$ are both dependent of each other. Therefore, an iterative process must be done so an initial L_o needs to be assumed to obtain $u*$ and compute the whole chain to obtain heat fluxes.

Usually when the terrain is flat, the height z is calculated as the mean height of the transmitter and receiver. However, in some cases the complexity of the terrain and the height of the vegetation produces that the estimated value of z is different from the real. In those cases it is necessary to calculate an effective height above the surface to be able to make use of the scintillometer theory (Bruin et al., 1995; Hartogensis et al., 2003; Van Kesteren, 2012). Although $f_{C_T^2}$ and $f_{C_q^2}$ are assumed to be universal, it has been shown that different MOST functions can cause up to 20% difference in H estimations (Hartogensis et al., 2003).

Wyngaard et al. (1971) found general similarity functions for unstable ($z/L_O < 0$) and stable ($z/L_o > 0$) conditions:

$$f_{C_{T\,unstable}^2}\left(\frac{z-d}{L_O}\right) = c_{T1}\left(1 - c_{T2}\frac{z-d}{L_O}\right)^{-2/3} \tag{A.39}$$

$$f_{C_{q\,unstable}^2}\left(\frac{z-d}{L_O}\right) = c_{q1}\left(1 - c_{q2}\frac{z-d}{L_O}\right)^{-2/3} \tag{A.40}$$

$$f_{C_{T\,stable}^2}\left(\frac{z-d}{L_O}\right) = c_{T1}\left(1 + c_{T2}\left(\frac{z-d}{L_O}\right)^{-2/3}\right) \tag{A.41}$$

$$f_{C_{q\,stable}^2}\left(\frac{z-d}{L_O}\right) = c_{q1}\left(1 + c_{q2}\left(\frac{z-d}{L_O}\right)^{-2/3}\right) \tag{A.42}$$

where c_{Ti} and c_{qi} are empirical coefficients.

Therefore, when temperature and humidity structural parameters have been obtained, sensible and latent heat fluxes can be computed. From C_T^2 and the universal functions, θ_* can be estimated through equation (A.31) if L_O is given. Since $q_* = (1 - q)L_vE/u_*$ and $\theta_* = H/\rho c_p u_*$, then L_vE and H can also be computed. Summarizing everything in one equation, H and L_vE can be estimated as:

$$H^2 = -\frac{\bar{\rho}^2 c_p^2 u_*^2 (z-d)^{2/3} C_T^2}{f_{C_T^2}} \tag{A.43}$$

$$L_vE^2 = -\frac{\bar{\rho}^2 L_v^2 u_*^2 (z-d)^{2/3} C_q^2}{(1-\bar{q})^2 f_{C_q^2}} \tag{A.44}$$

where ρ is the air density [kg/m^3].

Considerations

All the above theory is valid for weak dispersion, so it fails for strong turbulence and valid only for $\sigma_{ln^2(I)} \leq 0.3$. For values greater than this the term $ln(I)$ does not increase when C_n^2 increases, i.e. eddy fluctuations no longer cause amplitude fluctuations, which is called saturation. Optical scintillometers are the most susceptible to this because their Fresnel zone is small. To prevent this, it is necessary to increase the wavelength, i.e. to have larger eddies or shorten the length of the path, i.e. to see fewer eddies (van Kesteren, 2012).

Another thing to take into account is that, according to Stoffer (2018) when spectral analysis is done to distinguish different contributions to the signal it has been seen that real spectra have unwanted contributions that are not taken into account in the theoretical spectra at both high and low frequencies. At high frequencies they are contributions by absorption, while at low frequencies they are contributions by electronic noise (van Dinther et al., 2013).

This is why a band filter (BPF) is applied, including a high-pass filter (HPF) and a low-pass filter (LPF) in order to properly calculate C_n^2. Thus, all those frequency fluctuations under HPF and over LPF are filtered from the data and are not taken into account for the calculation of the parameters (Meijninger et al., 2006; Moene et al., 2005; Stoffer, 2018; Ward et al., 2015). The decision of which band filters to use is not trivial, as it must remove the unwanted but maintain the contributions associated with the fluxes. In addition, it is also necessary to consider the wind speed perpendicular to the trajectory, as this changes the range of frequencies in which the surface fluxes are located. High speeds cause them to be located around higher frequencies, while low speeds are located around lower frequencies.

This is addressed by Stoffer (2018), who looks for the HPF-LPF combination that makes a BPF more optimal considering the wind speed and other characteristics. He also reported that erratic spikes can be present in the spectra and are not always removed by the BPF. These spikes are not associated with the surface fluxes and they deteriorate the quality of the scintillometer measurements. As a summary Stoffer (2018) from his research recommends for MWS including a 100-200 Hz LPF, for LAS a HPF of 0.1 Hz and LPF of 100-200 Hz. He also recommends to always include a spike filter.

APPENDIX B: SPECTRAL ANALYSIS THEORY

Spectral analysis through Fourier technique is a key tool for analysing and describing turbulence. It allows to decompose a stationary random process into the sum of harmonic oscillations not correlated with random amplitudes and phases. Thus, it is possible to recognize and analyse those oscillations or frequencies that are most important for the signal, as well as to identify unwanted contributions.

Sinusoidal functions

Sinusoidal functions are the decomposition of a signal into a time series of a number of waves or oscillations with a certain frequency and amplitude. These waves are characterized by the period τ, the amplitude A_m, the phase φ_m and the frequency f_m (Hartogensis, 2019b). The function is constructed in time t such that

$$X_m(t) = A_m \sin(2\pi[f_m \cdot t + \phi_m]) \qquad \text{(A.45)}$$

The phase represents the offset of the sine wave on the time axis from the starting point of the total period. However, in order to solve the function and perform the decomposition it is necessary to consider the Nyquist theorem. This theorem implies that at least two samples are needed to solve a sine wave of a certain frequency (Hartogensis, 2019b).

Fourier and TTF time series

The Fourier series implies that the signal can be written as the sum of M sines and cosines such that

$$x(t_n) = A_0 + \sum_{m=1}^{M-1} A_m cos(w_m n \Delta t_s) + \sum_{m=1}^{M-1} B_m \sin(w_m n \Delta t_s) \qquad (A.46)$$

where A_0 is the average signal and A_m and B_m are the Fourier coefficients or the dependent amplitudes. A_m and B_m define the weights of the sinuses and cosines in the wave mode. The result of considering this as the sum of sine and cosine functions makes a Fourier series.

Based on this, Fourier transform is a technique that allows the determination of the coefficients A_m and B_m, from which the phase and amplitude of the wave can be known.

$$A_m = \frac{2}{N}\sum_{n=1}^{N} x[t_n]\cos(w_m n\Delta t_s) \qquad (A.47)$$

$$B_m = \frac{2}{N}\sum_{n=1}^{N} x[t_n]\sin(w_m n\Delta t_s) \qquad (A.48)$$

Thus, the spectrum is useful for identifying unwanted contributions to the signal variance, e.g. fluctuations due to turbulence from fluctuations associated with tower vibrations. However, to do so Fourier coefficients need to be scaled such that the area under the spectrum is proportional to the variance of the signal. Then the inverse transformation allows to filter out erroneous noises or erratic spikes and then return to a corrected time series (Hartogensis, 2019b).

Energy spectrum of a time series

Fourier transform allows to know the contribution per wave scale to the total variance of the signal. The energy spectrum and variance are given by:

$$S[m] = 2\big[x[m]\big]^2 = 2[(A_m)^2 + (B_m)^2] \qquad (A.49)$$

$$VAR(x) = \int S[m]dm = \sum_{m=1}^{M-1}(A_m)^2 + \sum_{m=1}^{M-1}(B_m)^2 \qquad (A.50)$$

As can be seen from the mathematical description, the energy spectrum ignores $m = 0$, i.e. the mean value. In the case of the upper limit, this is defined by the Nyquist frequency above which there are no wave scales that can be recovered.

Smoothing

When there is a smoothing effect, variance cannot be calculated as an integral of the spectrum. To solve this there are two methods according to Hartogensis (2019b):

1. The Welch method, which consists of shortening the time series so that the frequency range to be considered is smaller. However, it may not be possible to eliminate all the noise.

2. The filtration method, which must be used with care because it is easy to filter a portion of the spectrum, so it must be ensured that the integral over the spectrum does represent the variance of the signal.

To do this it is necessary to eliminate trends, because it avoids signals with discontinuities between the beginning and the end. It is also necessary to consider what is known as leakage, which is the contamination of certain frequencies as a result of the amplitude of neighbouring frequencies. This generates small discontinuities between the beginning and the end of the recording. To avoid this, the recording should be divided into windows by a hamming filter. This second option is the one used in this research.

APPENDIX C: DETAILED RESULTS

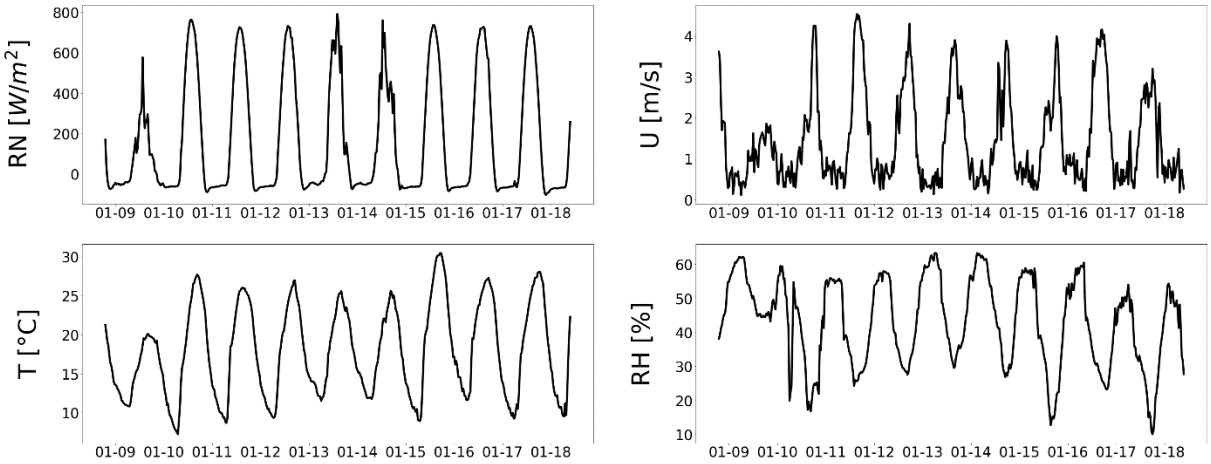

Figure A.3: (a) Net radiation registered by the meteorological station (b) Wind speed registered by Eddy Covariance system (c) Temperature registered by Eddy Covariance system (d) Relative humidity registered by Eddy Covariance system

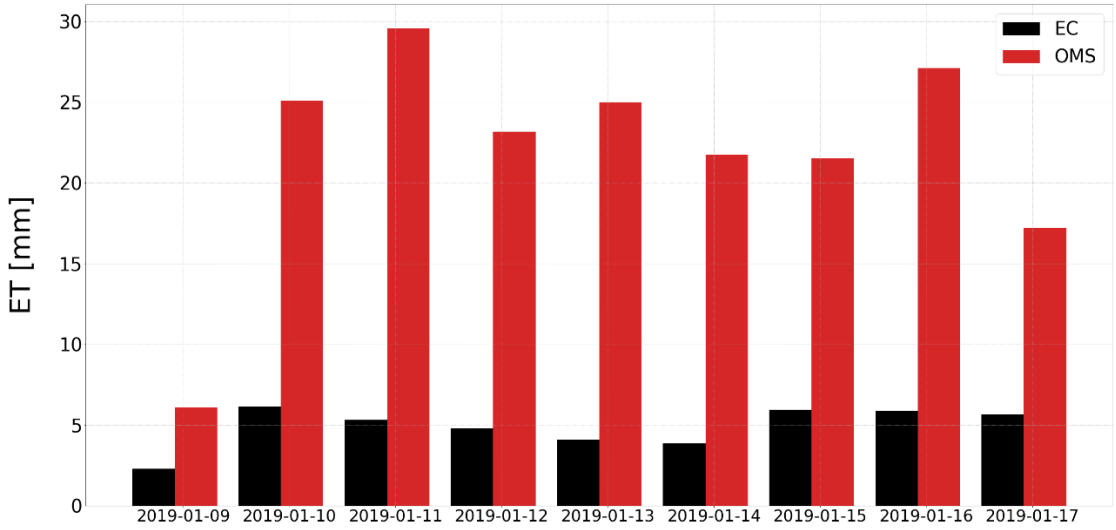

Figure A.4: EC and original OMS evapotranspiration.

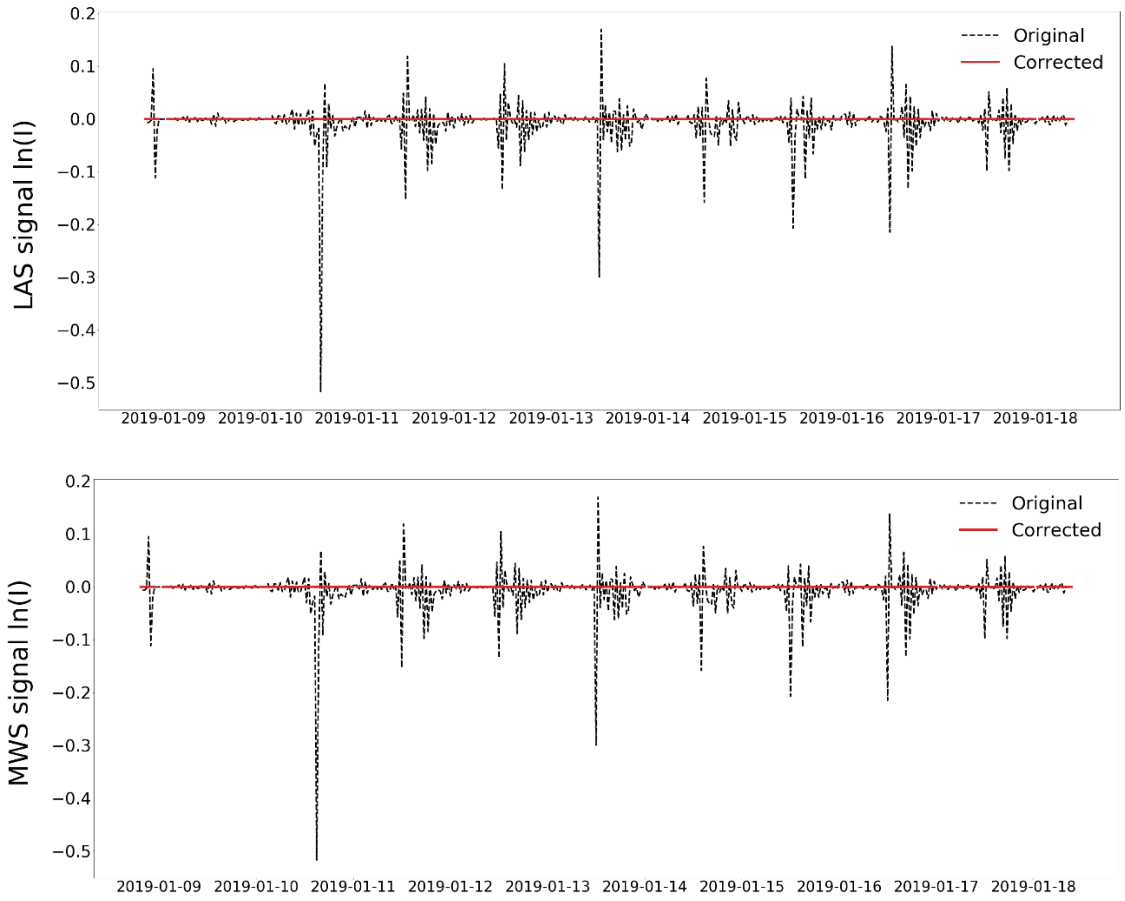

Figure A.5**:** (a) Comparison original and corrected LAS signal expressed as *ln*(*I*) (b) Comparison original and corrected MWS signal expressed as *ln*(*I*).

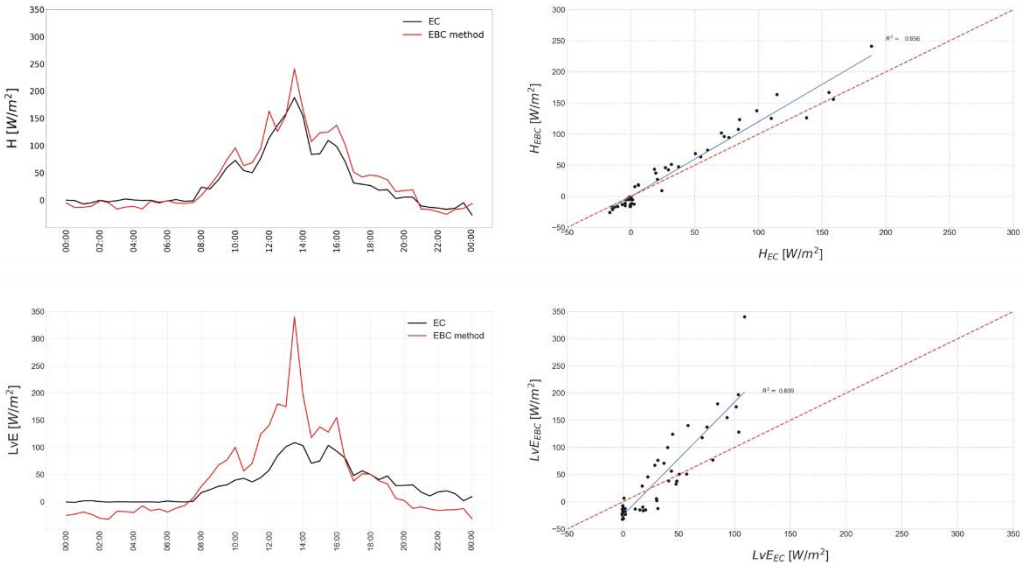

Figure A.6: Corrected heat fluxes and evapotranspiration from energy balance closure (Ezzahar et al., 2009) method compared with Eddy Covariance system for January 9th, 2019.

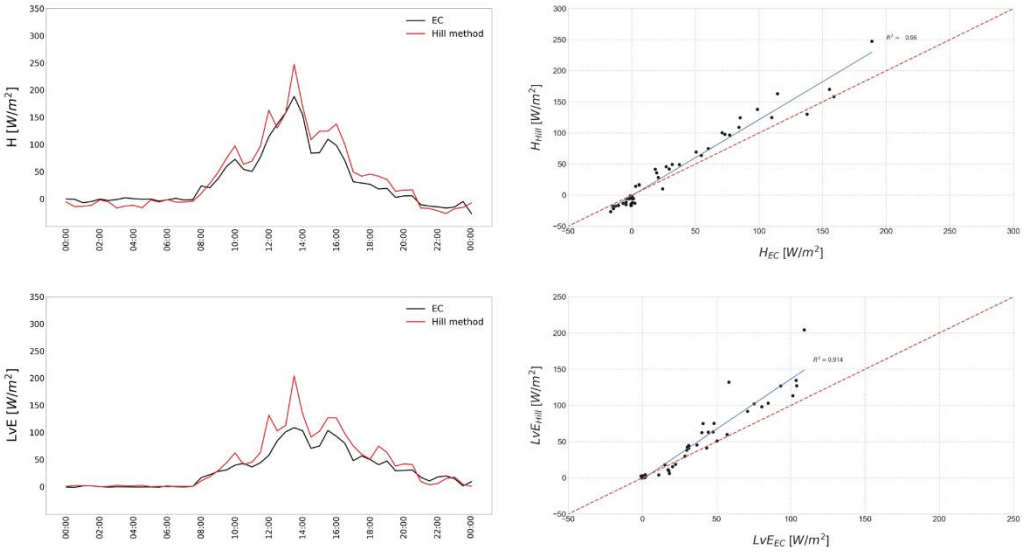

Figure A.7: Corrected heat fluxes and evapotranspiration from Hill (1997) method compared with Eddy Covariance system for January 9th, 2019.

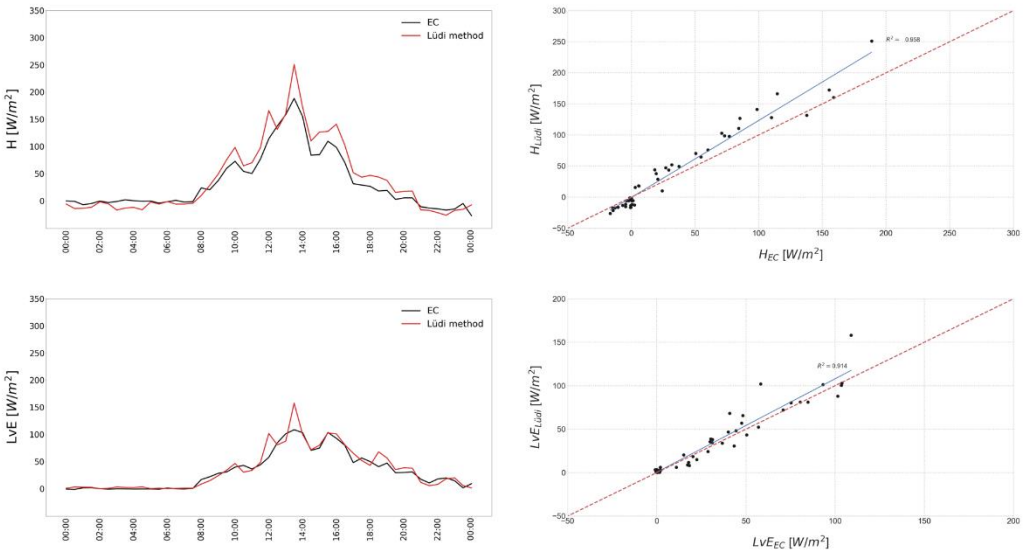

Figure A.8: Corrected heat fluxes and evapotranspiration from Lüdi et al. (2005) method compared with Eddy Covariance system for January 9th, 2019.

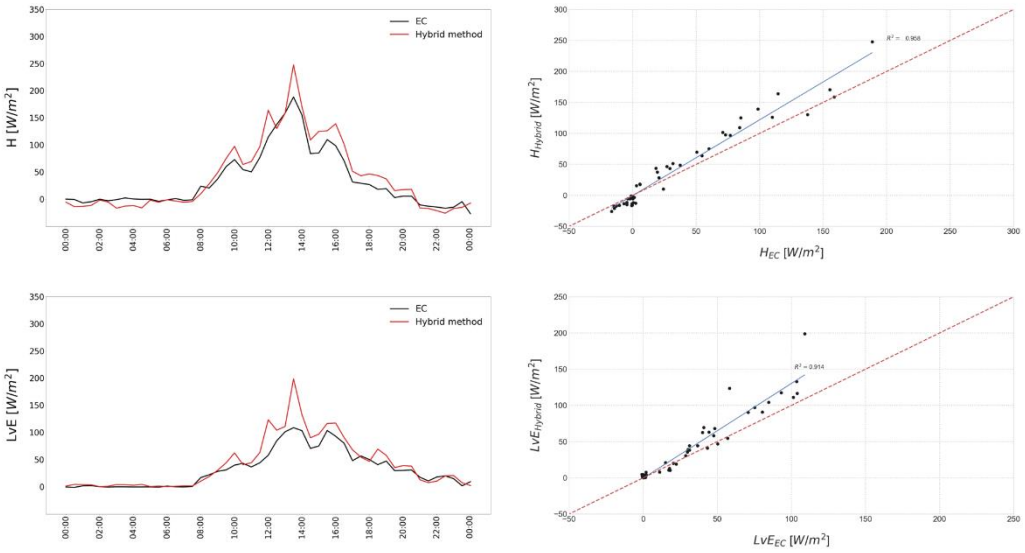

Figure A.9: Corrected heat fluxes and evapotranspiration from Stoffer (2018) hybrid method compared with Eddy Covariance system for January 9th, 2019.

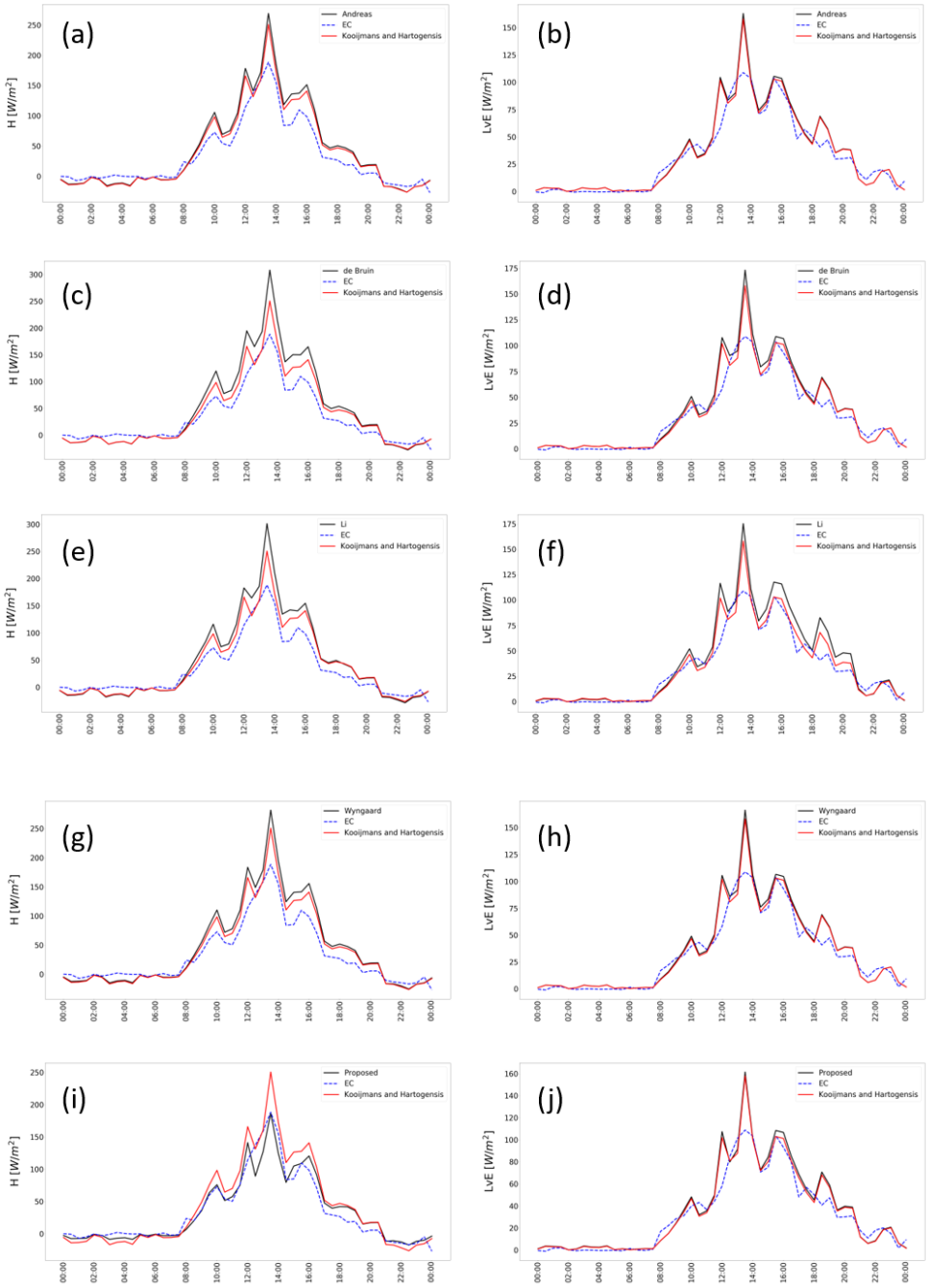

Figure A.10: Heat fluxes using Lüdi et al. (2005) method and (a) (b) Andreas (1988) (c) (d) de Bruin (1993) (e) (f) Li et al. (2012) (g) (h) Wyngaard (1971) (i) (j) Aguirre (2021- this work) similarity functions compared with Eddy Covariance system measurements and heat fluxes estimated using Kooijmans and Hartogensis (2016) similarity functions for January 9th, 2019.